A Very Impressive and Fancy Title for a Thesis

by

Giovanni Pederiva

Thesis

for the degree of

Master of Science

Faculty of Mathematics and Natural Sciences
University of Oslo

May 2018

Contents

Abstract

some abstract

Acknowledgements

Part I

Introduction to QCD and Lattice Field Theories

Chapter 1

A Primer on QCD in the Continuum

The Standard Model of particle physics (SM) is the theory of fundamental particles and their interactions. Three of the four known fundamental forces are described by it, the exception is Gravity, so that all phenomena regarding the Electromagnetic, Weak and Strong forces are included within the theory.
The SM describes quantized fields defined on all space-time whose excitations are commonly identified with particles. There are two categories of fields, depending on the spin statistic they can be: fermions, quarks or leptons in the SM, which are the constituents of matter; or bosons, which mediate the interactions between particles.

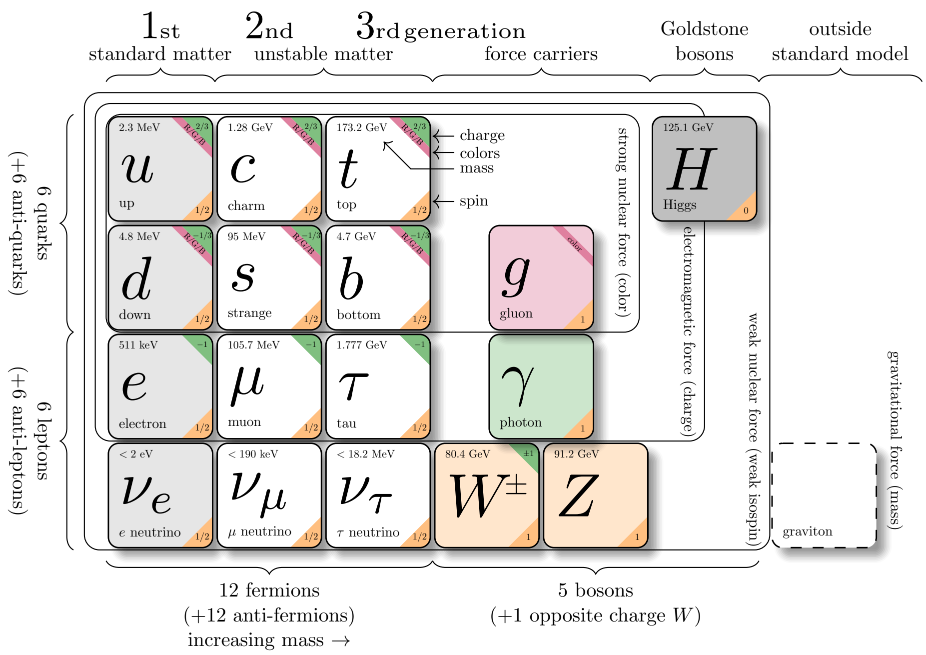

Figure 1.1: Summary of the particles on the Standard Model [1]

From a group theory point of view, the SM is the composition of three different local gauge symmetry groups, each associated with a fundamental force:

$$SU(3)_C \times \underbrace{SU(2)_L \times U(1)_Y}_{broken\ to\ \ SU(2)_W \times U(1)_Q} \tag{1.1}$$

The $U(1)_Q$ symmetry group is associated with the electromagnetic interaction and $SU(2)_W$ is the weak interaction. They both derive from the symmetry $SU(2)_L \times U(1)_Y$, which is spontaneously broken through the Higgs Mechanism, that defines the unified electroweak theory. Quantum Chromodynamics, commonly referred to as QCD, is the quantum field theory, contained in the SM, that describes the behavior of strongly interacting matter, that is quarks and gluons. It is a non-abelian gauge theory based on a $SU(3)$ symmetry group. The associated quantum number is called "color charge" which pictorially can assume the values of *red* (r), *green* (g), *blue* (b), *anti-red* ($\bar{r}$), *anti-green* ($\bar{g}$) or *anti-blue* ($\bar{b}$). In this chapter, we will discuss the QCD Lagrangian density, its properties and some of the major results of the theory. Some intermediate knowledge of Quantum Field Theory is assumed and derivations and proofs mainly follow the reasoning found in [2].

1.1 The QCD Lagrangian

In Quantum Field Theory (QFT) the characterizing equation of a theory is its Lagrangian density because it contains all the information about the fields that are involved, their properties and most importantly, their interactions. QCD is a non-abelian gauge theory based on the $SU(3)$ local gauge symmetry group. The simplest Lagrangian is the Yang-Mills Lagrangian:

$$\mathcal{L}_{QCD} = + \sum_{f=1}^{N_f} \bar{\psi}_f (i\gamma^\mu D_\mu - m_f)\psi_f - \frac{1}{4}(G^a_{\mu\nu})^2 \tag{1.2}$$

Here ψ_f and $\bar{\psi}$ represent the complex-valued fermion fields of flavor f, with mass m_f. These are associated with the quark fields and come in six flavors: u (up), d (down), s (strange), c (charm), b (bottom) and t (top). The second element in the Lagrangian is the Gluon Field Strength Tensor, $G^a_{\mu\nu}$. The two indices μ and ν are Lorentz and γ^μ are Dirac's matrices. a is the index of the generators of the gauge group, $SU(3)$ in this case. Note that Einstein's summing convention on repeated indices is implicit, for example when taking the square of the field strength tensor three sums are applied. The definition of $G^a_{\mu\nu}$ is:

$$G^a_{\mu\nu} = \frac{i}{g_0}[D_\mu, D_\nu] = \partial_\mu A^a_\nu - \partial_\nu A^a_\mu + g_0 f^{abc} A^b_\mu A^c_\nu \tag{1.3}$$

In this equation A^a_μ is the gluon field, that carries a Lorentz index and a group generator index, g_0 is the bare coupling constant of the strong interaction and the f^{abc} are the structure constants of $SU(3)$, which satisfy:

$$[t^a, t^b] = i f^{abc} t^c \tag{1.4}$$

with t^a being the generators of the algebra $\mathfrak{su}(3)$. The covariant derivative D_μ is defined to be:

$$D_\mu = \partial_\mu - ig_0 t^a A_\mu^a \tag{1.5}$$

With the information contained in the Lagrangian density, the behavior and the interactions of all fields are set.

1.1.1 Feynman Rules of QCD

A key element that is needed to perform perturbative calculations in a quantum field theory are Feynman Rules. These are a set of equations and rules that represent the propagation of fields and the interaction vertices of the theory. For the case of QCD, being a non-abelian gauge theory, some vertices represent interactions between gauge bosons only, as opposed to Quantum Electrodynamics, QED, that forbids photon-photon interactions.
To begin with, we need to write out all of the terms of the Lagrangian density individually. We assume only one quark flavor as no term in the Lagrangian can change this quantum number.

$$\begin{aligned}
\mathcal{L}_{QCD} &= \bar{\psi}(i\gamma^\mu D_\mu - m)\psi - \frac{1}{4}(G_{\mu\nu}^a)^2 \\
&= \bar{\psi}(i\gamma^\mu \partial_\mu + g_0\gamma^\mu t^a A_\mu^a - m)\psi \\
&\quad - \frac{1}{4}\left(\partial_\mu A_\nu^a - \partial_\nu A_\mu^a + g_0 f^{abc} A_\mu^b A_\nu^c\right)\left(\partial_\mu A_\nu^a - \partial_\nu A_\mu^a + g_0 f^{ade} A_\mu^d A_\nu^e\right) \\
&= \bar{\psi}(i\gamma^\mu \partial_\mu - m)\psi \\
&\quad - \frac{1}{4}\left(\partial_\mu A_\nu^a - \partial_\nu A_\mu^a\right)^2 \\
&\quad - g_0 f^{abc}\left(\partial_\mu A_\nu^a\right) A^{b\mu} A^{c\nu} \\
&\quad - \frac{1}{4} g_0^2 f^{abc} f^{ade} A_\mu^b A_\nu^c A^{d\mu} A^{e\nu} \\
&\quad + g_0 \gamma^\mu t^a A_\mu^a \bar{\psi}\psi
\end{aligned} \tag{1.6}$$

The first thing to do is to define the quark and gluon propagators, which can be obtained from the first and second terms respectively of the last equality:

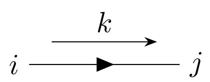

$$= \frac{i(\gamma^\mu k_\mu + m)}{k^2 - m + i\epsilon}\delta_{ij}$$

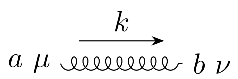

$$= -\frac{i}{k^2 + i\epsilon}\delta_{ab} g^{\mu\nu}$$

with $g^{\mu\nu}$ being the metric tensor of Minkovskian space-time. The third term in eq. (1.6) represents a three gluon vertex:

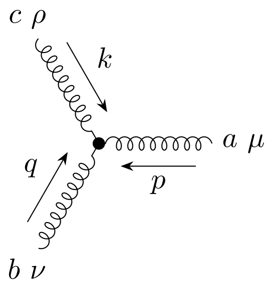

$$= g_0 f^{abc}\left[g^{\mu\nu}(p-q)^{\rho} + g^{\nu\rho}(q-k)^{\mu} + g^{\rho\mu}(k-p)^{\nu}\right]$$

Then the four-gluon vertex:

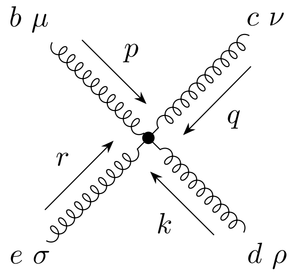

$$\begin{aligned} = -ig_0^2[\quad & f^{abe} f^{acd}(g^{\mu\nu} g^{\sigma\rho} - g^{\mu\rho} g^{\nu\sigma}) \\ + & f^{abd} f^{ace}(g^{\mu\nu} g^{\sigma\rho} - g^{\mu\sigma} g^{\nu\rho}) \\ + & f^{abc} f^{aed}(g^{\mu\sigma} g^{\nu\rho} - g^{\mu\rho} g^{\nu\sigma})] \end{aligned}$$

Finally we have the gluon-quark interaction vertex:

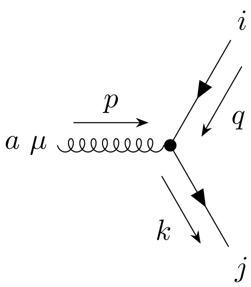

$$= ig_0 t^a \gamma^{\mu}$$

Note that the Lagrangian we considered, and the resulting Feynman rules, is over-simplified: the "full" Lagrangian contains terms from Faddeev-Popov ghosts, that are introduced to fix the problems that arise when fixing the gauge; and counter-terms from the renormalization procedure. Nevertheless, interesting qualitative features can be inferred from the Feynman rules: the fact that gluons interact with each other through the three- and four-gluon vertices; the non flavor-changing interaction between gluons and quarks, which decouples completely different quark flavors; the "color-changing nature" of the quark-gluon interaction, given by the t^a matrix in the vertex term that shows how the color state of a fermion is changed by the absorption or emission of a gluon.

1.1.2 Gauge Symmetry of the Lagrangian

The concept of gauge invariance is crucial in the construction of a discretized lattice theory from the continuum one, so it is worth considering how is is introduced. The QCD Lagrangian must be gauge invariant to be physical, not only on a global scale, but it must be locally invariant. Let's consider a quark field $\psi(x)$, which truly is a triplet of fermion fields each with different color quantum number:

$$\psi(x) = \begin{pmatrix} \psi_r(x) \\ \psi_b(x) \\ \psi_g(x) \end{pmatrix} \tag{1.7}$$

A local gauge transformation in the internal space of $SU(3)$ is a unitary transformation of this 3-component vector, a rotation in color space. Defining $\Omega(x)$ one such local transformation applied to $\psi(x)$ one has:

$$\psi(x) \to \psi'(x) = \Omega(x)\psi(x) \tag{1.8}$$

and for the Dirac adjoint:

$$\bar{\psi}(x) \to \bar{\psi}'(x) = \bar{\psi}(x)\Omega^\dagger(x) \tag{1.9}$$

The transformation can be parametrized in terms of some functions $\alpha^a(x)$, one for each generator of the group:

$$\Omega(x) = \exp[i\alpha^a(x)t^a] \tag{1.10}$$

This internal space rotation if applied to the simple Dirac free-field Lagrangian would generate an additional term:

$$\begin{aligned} \mathcal{L}_{Dirac} = \bar{\psi}(i\gamma^\mu\partial_\mu - m)\psi \ \to \ \mathcal{L}'_{Dirac} &= \bar{\psi}\Omega^\dagger(i\gamma^\mu\partial_\mu - m)(\Omega\psi) \\ &= \bar{\psi}'(i\gamma^\mu\partial_\mu - m)\psi' + i\bar{\psi}'\gamma^\mu\psi(\partial_\mu\Omega) \end{aligned} \tag{1.11}$$

The extra term implies that Dirac lagrangian is not gauge invariant. In order to fix this problem a new field $A_\mu(x)$, the gauge field, and it is convention to include it into the definition of the covariant derivative, so that ∂_μ becomes $D_\mu = \partial_\mu - ig_0A_\mu(x)$, as previously stated; D_μ represents the derivative along the tangent vectors of the manifold on which the field is defined. The field $A_\mu(x)$ is algebra-valued and, to be consistent with the previous section one need to project it on a basis of generators of the group: $A_\mu(x) = A^a_\mu(x)t$ (remember the implicit sum).
The transformation rule for $A_\mu(x)$ is fixed in order to cancel the extra term in eq. (1.11) exactly, such that:

$$D_\mu\psi \to (D_\mu\psi)' = (\partial_\mu - ig_0A'_\mu(x))\psi' = \Omega(D_\mu\psi) \tag{1.12}$$

and this fixes the transformation for $A_\mu(x)$ to be:

$$A_\mu(x) \to A'_\mu(x) = \Omega\left[A_\mu(x) + \frac{i}{g_0}\Omega^\dagger\partial_\mu\Omega\right]\Omega^\dagger \tag{1.13}$$

we can see that the last term contributes effectively to the Lagrangian as $-i\bar{\psi}'\gamma^\mu\psi(\partial_\mu\Omega)$, which is what we wanted to cancel. For an infinitesimal transformation we can expand the matrix Ω in powers of α as $\Omega(x) = \exp[i\alpha^a(x)t^a] \approx 1 + i\alpha^a(x)t^a$ and get the following for the gauge field transformation, for a single component:

$$A^a_\mu(x) \to A'^a_\mu(x) = A^a_\mu(x) + \frac{i}{g_0}\partial_\mu\alpha^a(x) + f^{abc}A^b_\mu(x)\alpha^c(x) \tag{1.14}$$

which is the last element needed. One can now look at all the possible gauge invariant objects that can be constructed with the fields ψ and A of dimension 4, the same of the Lagrangian. Apart from the one already present in the Dirac Lagrangian with the covariant derivative, there are only two additional terms that are gauge invariant and of dimension 4 and they both can be taken by considering the gauge field tensor:

$$G^a_{\mu\nu} \equiv \frac{i}{g_0}\left[D_\mu, D_\nu\right] = \partial_\mu A^a_\nu - \partial_\nu A^a_\mu + g_0 f^{abc} A^b_\mu A^c_\nu \tag{1.15}$$

this is clearly gauge invariant since it is the commutator of covariant derivatives and it has dimension 2. One can now construct the gauge field kinetic term, the well known $-\frac{1}{4}(G^a_{\mu\nu})^2$ and reconstruct eq. (1.2). However, there is an additional term, not included in the QCD Lagrangian, that is the "dual term", or "theta term" which will be interesting further in the work. It is defined as $\theta G^a_{\mu\nu}\tilde{G}^{a\mu\nu}$ where $\tilde{G}^{a\mu\nu} = \epsilon^{\mu\nu\rho\sigma} G_{a\rho\sigma}$ is the dual of the field tensor and $\epsilon_{\mu\nu\rho\sigma}$ the anti-symmetric Levi-Civita tensor of rank 4. With it the Lagrangian becomes:

$$\mathcal{L}_{QCD} = -\frac{1}{4}(G^a_{\mu\nu})^2 + \bar{\psi}(i\not{D} - m)\psi + \theta G^a_{\mu\nu}\tilde{G}^{a\mu\nu} \tag{1.16}$$

The theta term is usually neglected because there is no experimental evidence of it, but in principle it cannot be excluded. It is the simplest CP violating term that can be added to the QCD Lagrangian and for this is of particular interest in the study of $\not{C}\not{P}$ phenomena, like the nucleon electric dipole moment (EDM)[3].

1.2 General Properties of QCD

Quantum Chromodynamics exhibits a set of features as a theory that is common to all non-abelian gauge theories. We have already seen one, that is the direct interaction of the gauge bosons, something that is not allowed in abelian theories as QED. Other interesting properties emerge when trying to renormalize the theory and are in general linked to the fixing of the scale, which leads to the concept of running coupling. In the particular case of QCD, the coupling constant at in a low-energy regime leads to Confinement, while in the high-energy limit Asymptotic Freedom emerges.

1.2.1 Running Coupling

The Renormalization Group Equation (RGE) defines the rate at which the renormalized coupling g varies as the renormalization scale of μ changes, through the beta function of the coupling constant, $\beta(g)$.

$$\beta(g) = \frac{d}{d\log(\mu)} g(\mu) \tag{1.17}$$

For a generic non-abelian theory $SU(N)$ one can expand the β function in orders of g as:

$$\beta(g) = b_0 g^3 + b_1 g^5 + b_2 g^7 + \dots \tag{1.18}$$

One can then integrate up to arbitrary order eq. (1.17) and get an expression for $g(\mu)$. The coefficients b_i are obtained from computing contribution of higher and higher diagrams to the coupling. The value of b_0, from 1-loop corrections, is:

$$b_0 = -\frac{1}{(4\pi)^2}\left(\frac{11}{3}N - \frac{2}{3}N_f\right) \tag{1.19}$$

Here N is the gauge group $SU(N)$dimension and N_f the number of flavors of the fermions. The minus sign in front implies that any non-abelian theory with a sufficiently small number of fermions, less than $\frac{11}{2}N$ (that is 16 for QCD), is "asymptotically free", meaning that at high energy the coupling vanishes and particles don't feel any interaction.
The RGE is usually expressed in terms of the analog of the fine structure-constant for the strong force, $\alpha_s = g^2/4\pi$. The first order solution is given by plugging eq. (1.19) into eq. (1.17) and integrating. In terms of α_s at a scale μ we get:

$$\alpha_s(\mu) = \frac{\alpha_s^0}{1 + \frac{b_0\alpha_s^0}{4\pi}\log(\mu^2/M^2)} \tag{1.20}$$

here α_s^0 is the value of the coupling at an energy M, which is set by the integration. The typical choice for M when measuring experimentally the running coupling is the mass of the Z boson, where QCD can be compared relatively simply to the other forces and experimental precision is high. The coupling depends on an arbitrarily chosen renormalization point M, so a convenient choice is rewrite the equation in simpler way defining a momentum scale Λ that satisfies:

$$1 = \frac{b_0\alpha_s^0}{4\pi}\log(M^2/\Lambda^2) \tag{1.21}$$

This simplifies eq. (1.20) to its well-known form, correct up to one loop corrections:

$$\alpha_s(\mu) = \frac{4\pi}{b_0\log(\mu^2/\Lambda^2)} \tag{1.22}$$

In fig. 1.2 a higher order approximation of $\alpha_s(\mu)$ is plotted against some experimental values. In section 3.4.1 we will show a more precise result, correct up to 4 loop corrections, of this result. The momentum scale, often referred to as Λ_{QCD}, is the energy at which the interactions become strong. Experimental values [5] suggest that $\Lambda_{QCD} \approx 200 - 300$ MeV, meaning that perturbation theory can be safely applied form momenta roughly above the 1 GeV scale, where $\alpha_s \approx 0.4$.
One of the main goals for this thesis is to find a simple and not expensive way to estimate the mass scale parameter Λ from lattice calculations, in this work on pure Yang-Mills theory, that means with no fermion flavors, and in prospect for QCD with 2 or $2 + 1$ dynamical fermions.

Asymptotic Freedom

Equation (1.22) is a clear indication that QCD at high energies has a small coupling. Asymptotic freedom is the property of gauge theories, QCD is usually the example of it, that causes the interactions between the fields do become weaker as the energy scale increases and this is because

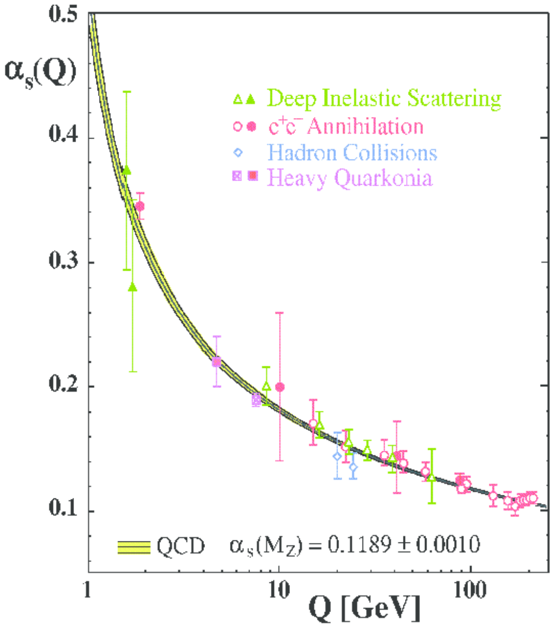

Figure 1.2: The strong coupling as a function of the energy scale, The data points are experimental results; the black solid line and yellow bands represent the QCD prediction using the reported value of the coupling at the mass of the Z boson (α_s^0 in our notation). Image from [4]

of the inverse log dependence of the coupling on the energy. This is, for example, one of the bases on which Grand Unification Theories (GUT) are based on, the fact that there exists an energy scale at which the strong force has a coupling equivalent to the one of the electroweak interaction.
The discovery of asymptotic freedom by Gross, Wilczek and Politzer [6][7], was used as an indication that QCD is indeed the correct theory of the strong interaction in the late Seventies, when the fundamental theory was still debated.
Asymptotically free theories can be analyzed perturbatively at sufficiently large energies and are believed to be consistent up to any energy scale.

Confinement

In general, color charged particles cannot be isolated, so that quarks and gluons are not detectable alone, but always in the form of hadrons: colorless objects formed of multiple quarks, mesons (quark-antiquark) and hadrons (three quarks or three anti-quarks). Glueballs, combinations of gluons such that the total is colorless, are also in principle allowed, but have not been observed yet. Confinement is the phenomenon for which it is not possible to isolate a color charge, single quarks or gluons, from a hadron without producing other new hadrons. Single colored particles in a very small time scale undergo hadronization, the process of spawning new quarks or anti-quarks from the vacuum to balance the total color charge and produce colorless matter. This is the reason for the fundamentally different nature of the strong force compared

to the other forces, no perturbative expansion can be made at low energies. The exact proof of how this links with the color confinement of QCD is yet not known, but qualitatively it can be explained by the fact that the gauge bosons of the theory, the gluons, carry color charge just like the quarks.
At low energy scales from eq. (1.22) we can infer that the coupling constant increases exponentially, so particles that have energies comparable to the energy scale Λ_{QCD} interact very strongly with the gauge field and any other particle. This implies, for example, that the force between two particles does not vanish for long distances, but instead it increases. The usual picture is to consider the gluons being exchanged by two quarks at rest. These gluons would form flux-tubes between the sources that, if stretched by separating the quarks, eventually store enough energy to make a quark-anti-quark pair energetically favorable.

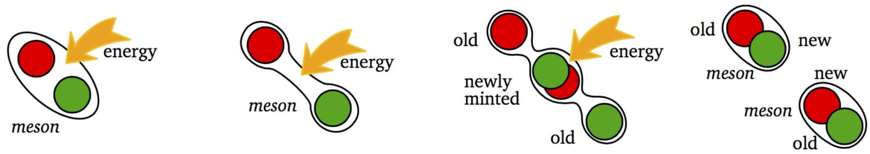

Figure 1.3: Representation of confinement using flux-tubes . As two color sources are pulled apart, the energy stored in the color field between the sources increases so much that a $q\bar{q}$ pair is formed from the vacuum energy.

One could also look at the inverse of the energy scale, which is a distance in natural units, of roughly $\Lambda_{QCD}^{-1} \approx 1fm$, that is approximately the size of light hadrons, a further proof that quark sources cannot be torn apart easily.
The strong low-energy interaction is the cause for the large discrepancy between the mass of the baryons and the mass of their constituent quarks. For the proton for example, the quark masses (2 up-quarks and 1 down-quark) give a total of 10 MeV, while the mass of the proton is 938 MeV. This means that the 99% of the mass of the proton is given by the quark and gluon binding energy.

1.3 Methods and Regimes of Chromodynamics

Given the very different behaviors of the strong force at different energy scales, QCD needs to be dealt with in various ways depending on the scale of interest. At high energies, perturbation theory can be applied safely, but at low ones no expansion in the coupling constant can be made.

Perturbative QCD

At high energies, like the scale of the large particle accelerators that are currently available, the QCD coupling constant is sufficiently small to allow analytical calculations of Feynman diagrams to be meaningful. Hadronization is neglected as the time scale is small enough to consider it a post-collision process. For example, at a scale where the strong force is comparable to the electroweak interaction, the cross section of $e^+e^- \to hadrons$ compared to that of $e^+e^- \to \mu^+\mu^-$ can be used to measure the number of quark flavors that are active below that energy. Figure (1.4) the perturbative QCD cross section for the process is shown compared to experimental data.

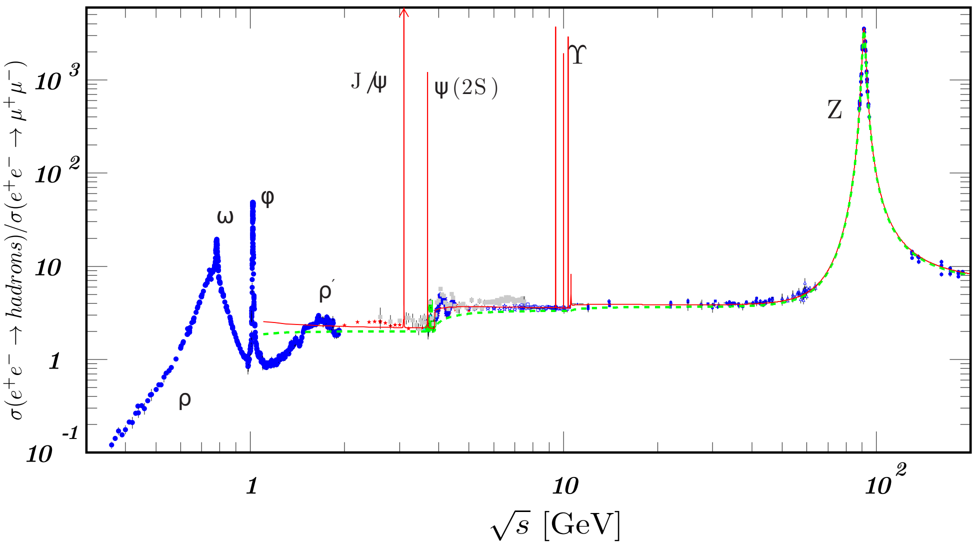

Figure 1.4: Ratio of the experimental cross section of $e^+e^- \to$ hadrons and $e^+e^- \to \mu^+\mu^-$ as collected by the Particle Data Group. Naive quark model is the dashed green line and pQCD results are also shown as a solid red line. pQCD appear to agree well to experiment in non resonant regions of the energy spectrum. The steps are given by the energy threshold of different quark flavors.

Lattice Methods

To deal with the non-perturbative sector of the strong interaction the most widespread approach is to use numerical simulations, in particular, lattice methods, so it is common to refer to it as Lattice QCD. The main idea, which will be expressed more in detail in Chapter 2, is to discretize space-time and evaluate the field only at fixed sites on a hyper-cubic lattice, physical quantities are then computed stochastically on ensembles of such gauge fields. This approach, however, is very expensive from a computational point of view and so far no calculation at physical quark masses with a sufficiently small lattice spacing, in principle closer to the continuum theory, have been performed.

Effective Field Theories

An interesting problem is to link QCD directly with nuclear forces, that are long-range remnants of the strong interaction at a hadron level. The problem is of high interest because there is yet no fundamental theory of nuclear interactions from first principles. The most common

approach is to define an Effective Field Theory, starting from a low energy approximation of chromodynamics, that preserves most of the symmetries of the underlying theory.
Chiral EFT (χEFT) is one of the most popular of such theories; it starts from considering nucleons as a fundamental $SU(2)$ group in isospin and describes the interactions between them through the exchange of pions [8]. It promotes particles that are not fundamental in QCD to the basic blocks of a low-energy effective Lagrangian, with nucleons as the fermion fields and pions as Nambu-Goldstone bosons of the theory. Its Lagrangian is constructed in a systematic manner considering all possible interaction vertices between hadrons:

$$\mathcal{L}_{\chi EFT} = \mathcal{L}_{\pi\pi} + \mathcal{L}_{\pi N} + \mathcal{L}_{NN} + \text{ (three hadron terms) } + \dots \tag{1.23}$$

where $\mathcal{L}_{\pi\pi}$ is the term describing the dynamics between pion, $\mathcal{L}_{NN}$ the term for interactions between two nucleons, $\mathcal{L}_{\pi N}$ the one between one pion and one nucleon and so on. Each term is further expanded in powers of Q/Λ_χ where Q is the pion momentum and Λ_χ is the energy scale at which the theory breaks down because of the of the pions acquiring an energy comparable to the mass of the nucleons. One constructs order by order all possible terms:

$$\begin{aligned} \mathcal{L}_{NN} &= \mathcal{L}_{NN}^{(0)} + \mathcal{L}_{NN}^{(2)} + \mathcal{L}_{NN}^{(4)} + \dots \\ \mathcal{L}_{\pi N} &= \mathcal{L}_{\pi N}^{(1)} + \mathcal{L}_{\pi N}^{(2)} + \mathcal{L}_{\pi N}^{(3)} + \mathcal{L}_{\pi N}^{(4)} + \dots \\ \mathcal{L}_{\pi\pi} &= \mathcal{L}_{\pi\pi}^{(2)} + \mathcal{L}_{\pi\pi}^{(4)} + \dots \end{aligned} \tag{1.24}$$

one then computes all possible diagrams order by order and truncates the expansion when needed. This is mostly useful for computing reduced matrix elements for many-body nuclear calculations.

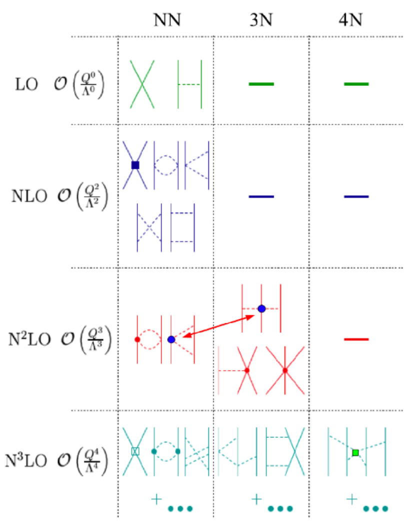

Figure 1.5: Diagrams of the leading order terms in χEFT. [9]

One interesting remark, as seen in fig. 1.5 is that the approach of χEFT spontaneously generates interaction matrix elements for three or more nucleons.

Chapter 2

Lattice Field Theories and Lattice QCD

Lattice QCD is one of the main Lattice Field Theories. It deals with the strong force at low energies, handling non-perturbative calculations in a numerical way. The idea of discretizing space-time in a lattice and perform calculations of field theories was proposed by Wilson in 1974 [10] as an alternative method to explain confinement. It has proven to be the most systematic approach to non-perturbative theories like QCD. In this chapter we will describe briefly how this discretization procedure is performed and some of the main computational strategies that are involved.

2.1 Discretizing Field Theories

The starting point for Lattice QCD is Feynman's path-integral formalism, but expressed in Euclidean space-time, through a Wick rotation. An observable of some field ϕ is then given by:

$$\langle O[\phi]\rangle = \frac{1}{Z[\phi]} \int \mathcal{D}[\phi]\ O[\phi] e^{-S[\phi]} \tag{2.1}$$

and the euclidean correlator of two quantities $O_1[\phi]$ and $O_2[\phi]$ between times t_1 and t_2 is:

$$\langle O_1[\phi](t_1) O_2[\phi](t_2)\rangle = \frac{1}{Z[\phi]} \int \mathcal{D}[\phi]\ O_1[\phi(t_1)] O_2[\phi(t_2)] e^{-S[\phi]} \tag{2.2}$$

where the partition function $Z[\phi]$ is defined as:

$$Z = \int \mathcal{D}[\phi]\ e^{-S[\phi]} \tag{2.3}$$

and $S[\phi]$ is the euclidean action of the field:

$$S[\phi] = \int d^4x \mathcal{L}[\phi] \tag{2.4}$$

Evaluating path-integrals is not possible in general with analytical tools so, in order to allow numerical computations, the Euclidean space-time is discretized on a hyper-cubic lattice $L = (L_x, L_y, L_z, L_t)$. The choice of the lattice spacing, usually denoted a, is arbitrary, but most often it is chosen to be equal for all dimensions. If we then define a lattice site $n = (n_x, n_y, n_z, n_t)$ where all the ns represent the coordinates of a point in the lattice Λ, our fields are constrained to have values on the points an instead of on a continuum space-time x^μ.

$$\phi(x) \xrightarrow{discretization} \phi(an) \tag{2.5}$$

2.1.1 The Harmonic Oscillator Example

Should I include this?

2.2 Discretization of QCD on the Lattice

In the case of QCD there are two types of field at play, the gluon gauge field A and the N_f fermionic quark fields ψ. In order to perform numerical calculations on the lattice, it is necessary to discretize the Euclidean action for both fields.
LagrIn this section the discretization is performed following a structure that resembles section 1.1.2, that is to start from the fermion fields and imposing gauge invariance.

2.2.1 Naïve Discretization of Fermions

In this section the fermion discretization procedure found in [11] is followed, but also some elements from [12], quoting the main intermediate steps that lead to the formulation of Lattice QCD. The starting point is the fermionic euclidean action in the continuum:

$$S_F[\psi, \bar{\psi}] = \int d^4x \bar{\psi}(x)(\gamma_\mu \partial^\mu + m)\psi(x) \tag{2.6}$$

now we discretize the euclidean space-time on a lattice Λ of spacing a, each point will be denoted with n. The partial derivative can be turned into the central finite difference between neighboring points along the direction of the derivative:

$$\partial_\mu \psi(x) \rightarrow \frac{\psi(n+\hat{\mu}) - \psi(n-\hat{\mu})}{2a} \tag{2.7}$$

The discretized fermion action is then the sum of the lagrangian density over all lattice sites multiplied by the unit volume a^4:

$$S_F[\psi, \bar{\psi}] = a^4 \sum_{n\in\Lambda} \bar{\psi}(n) \left[\sum_{\mu=1}^{4} \gamma_\mu \frac{\psi(n+\hat{\mu}) - \psi(n-\hat{\mu})}{2a} + m\psi(n) \right] \tag{2.8}$$

As we did in section 1.1.2 we try to apply a local gauge transformation $\Omega(n)$ to the field. It is simple to show that some terms of the derivative in the action are not gauge invariant:

$$\bar{\psi}(n)\psi(n \pm \hat{\mu}) \to \bar{\psi}(n)\Omega^\dagger(n)\Omega(n \pm \hat{\mu})\psi(n \pm \hat{\mu}) \tag{2.9}$$

The problem is in the way the derivative was discretized and the solution is the introduction of an additional field as in 1.1.2 that has the correct transformation laws. This field must transform under a local gauge transformation in a way that connects the values of the fermion field at two different lattice sites Because of this property we denote the auxiliary field as "link variables", later the matching with the gauge filed will be introduced, and by convention it is written as $U(n, n + \hat{\mu}) = U_\mu(n)$. Furthermore, it must depend on the orientation along the μ direction, from eq. (2.9):

$$U(n, n - \hat{\mu}) \equiv U_{-\mu}(n) = U_\mu(n - \hat{\mu})^\dagger \tag{2.10}$$

In particular, we want it to transform as:

$$\begin{aligned} \bar{\psi}(n)U_\mu(n)\psi(n + \hat{\mu}) &\to \bar{\psi}(n)\Omega^\dagger(n)U'_\mu(n)\Omega(n + \hat{\mu})\psi(n \pm \hat{\mu}) \\ \bar{\psi}(n)U_{-\mu}(n)\psi(n - \hat{\mu}) &\to \bar{\psi}(n)\Omega^\dagger(n)U'_{-\mu}(n)\Omega(n + \hat{\mu})\psi(n \pm \hat{\mu}) \end{aligned} \tag{2.11}$$

from which we infer that:

$$\begin{aligned} U_\mu(n) &\to U'_\mu(n) = \Omega(n)U_\mu(n)\Omega^\dagger(n + \hat{\mu}) \\ U_{-\mu}(n) &\to U'_{-\mu}(n) = \Omega(n)U_{-\mu}(n)\Omega^\dagger(n - \hat{\mu}) \end{aligned} \tag{2.12}$$

the field $U_\mu(n)$ is an $SU(3)$ valued field, that can be intuitively thought of as a set of oriented links between the sites of the lattice. A visual representation is given in fig. 2.1,

Figure 2.1: Schematic representation of the link variables $U_\mu(n)$ and $U_{-\mu}(n)$ on the lattice.

With this results we can write a gauge invariant lattice fermion action as:

$$S_F[\psi, \bar{\psi}] = a^4 \sum_{n\in\Lambda} \bar{\psi}(n) \left[\sum_{\mu=1}^{4} \gamma_\mu \frac{U_\mu(n)\psi(n + \hat{\mu}) - U_{-\mu}(n)\psi(n - \hat{\mu})}{2a} + m\psi(n) \right] \tag{2.13}$$

2.2.2 The Gauge Transporter and the Wilson Loop

For a more formal definition of the link variables we can look at the continuum gauge transporter. This is the path-ordered product, denoted with $\mathcal{P}$ of a gauge field $A_\mu(x)$ along some curve $\mathcal{C}$ between two points x and y in space-time:

$$G(x, y) = \mathcal{P} \exp \left(i g_0 \int_{\mathcal{C}} A_\mu(x') dx'^\mu \right) \tag{2.14}$$

An important thing to note now is that gauge transporter belongs to the gauge group, $SU(3)$ for QCD, and not to the algebra, $\mathfrak{su}(3)$. Up to order $\mathcal{O}(a)$ the integral on the straight line connecting two points on the lattice can be approximated with $aA_\mu(n)$ for small lattice spacings. For convenience the gauge filed is scaled by a factor $1/g_0$, giving:

$$\tilde{A}_\mu(x) = \frac{1}{g_0} A_\mu(x) \tag{2.15}$$

but for notation's sake we'll drop the tilde from now on. One is then left with:

$$\begin{aligned} G(n, n+\hat{\mu}) \equiv U_\mu(n) \quad &= \exp(iaA_\mu(n)) = \mathbb{1} + iaA_\mu(n) + \mathcal{O}(a^2) \\ G(n, n-\hat{\mu}) \equiv U_{-\mu}(n) &= \exp(-iaA_\mu(n)) = \mathbb{1} - iaA_\mu(n-\hat{\mu}) + \mathcal{O}(a^2) \end{aligned} \tag{2.16}$$

where in the second equation, for the negative direction, the approximation is taken on the arrival point instead on the initial one. With this definition is easy to see the relation we just stated earlier on the direction change:

$$U(n, n-\hat{\mu}) = U_{-\mu}(n) = U^\dagger_\mu(n) \tag{2.17}$$

In the continuum case it can be shown, in [2] for example, that the trace of a gauge transporter that has the same start and final point, a Wilson Loop, is gauge invariant. On the lattice the minimal Wilson loop is just a square on a fixed plane $\mu\nu$, and we call this a Plaquette:

$$\begin{aligned} P_{\mu\nu}(n) &= U_\mu(n) U_\nu(n+\hat{\mu}) U_{-\mu}(n+\hat{\mu}+\hat{\nu}) U_-\nu(n+\hat{\nu}) \\ &= U_\mu(n) U_\nu(n+\hat{\mu}) U^\dagger_\mu(n+\hat{\nu}) U^\dagger_\nu(n) \end{aligned} \tag{2.18}$$

a pictorial representation is given in fig. 2.2.

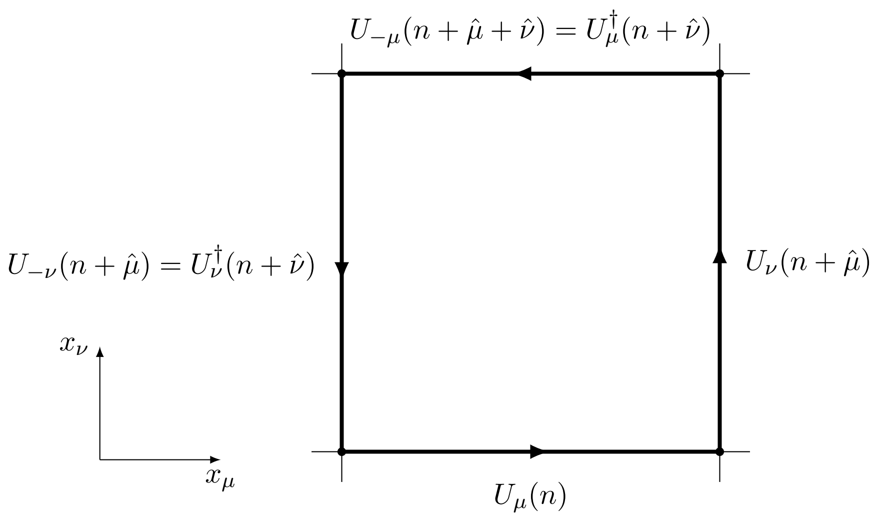

Figure 2.2: The Plaquette, as defined on the lattice, it terms of the oriented product of the link variables of a minimal square in the plane $\mu\nu$.

This allows us to write using eq. (2.16) and applying the Baker-Campbell-Hausdorff formula to deal with the product of matrix exponentials:

$$
\begin{aligned}
P_{\mu\nu}(n) = \exp\Bigg[& iaA_\mu(n) + iaA_\nu(n+\hat{\mu}) - iaA_\mu(n+\hat{\nu}) - iaA_\nu^\dagger(n) - \frac{a^2}{2}[A_\mu(n), A_\mu(n+\hat{\mu})] \\
& - \frac{a^2}{2}[A_\nu(n+\hat{\nu}), A_\nu(n)] + \frac{a^2}{2}[A_\mu(n), A_\nu(n)] + \frac{a^2}{2}[A_\nu(n+\hat{\mu}), A_\mu(n+\hat{\nu})] \\
& + \frac{a^2}{2}[A_\mu(n), A_\mu(n+\hat{\nu})] + \frac{a^2}{2}[A_\nu(n+\hat{\mu}), A_\nu(n)] + \mathcal{O}(a^3)\Bigg]
\end{aligned} \tag{2.19}
$$

Now the terms that are shifted from the site n can be expanded as:

$$
A_\mu(n+\hat{\nu}) = A_\mu(n) + a\partial_\nu A_\mu(n) + \mathcal{O}(a^2) \tag{2.20}
$$

and with this substitution most terms cancel and one has:

$$
\begin{aligned}
P_{\mu\nu}(n) &= \exp\left[ia^2(\partial_\mu A_\nu(n) - \partial_\nu A_\mu(n) + i[A_\mu(n), A_\nu(n)]) + \mathcal{O}(a^3)\right] \\
&= \exp\left[ia^2 G_{\mu\nu}(n) + \mathcal{O}(a^3)\right]
\end{aligned} \tag{2.21}
$$

Where we recovered the gauge field strength tensor $G_{\mu\nu}$. This term can be used to build the euclidean lattice action term for the gluons. In particular, to be able to recover the continuum action, we would like a term of the form:

$$
S_G[U] = \frac{a^4}{2g^2}\sum_{n\in\Lambda}\sum_{\mu\nu}\mathrm{Tr}(G_{\mu\nu}(n)^2) \xrightarrow{a\to 0} \frac{1}{4g^2}\int d^4x G_{\mu\nu}(x)^2 = S_G[A] \tag{2.22}
$$

Note that the $1/g_0^2$ term, that might seem strange since it is not in the known continuum Lagrangian is given by the scaling of the field in eq. (2.15). Up to order $\mathcal{O}(a^2)$ this can be obtained, in terms of the link variables, by:

$$
S_G[U] = \frac{2}{g^2}\sum_{n\in\Lambda}\sum_{\mu<\nu}\mathrm{ReTr}(\mathbb{1} - P_{\mu\nu}(n)) \tag{2.23}
$$

Higher order corrections to this action can be computed analytically by considering higher orders in the BCH expansion in eq. (2.19) and in the exponential expansion in eq. (2.21).

2.2.3 Lattice Fermions

The discretization of fermions as discussed in the previous section is incomplete as it leads to unphysical results. It becomes evident if one considers the Fourier transform of the propagator. Let's first rewrite 2.13 in a more compact way, introducing the lattice Dirac propagator $M_{xy}[U]$.

$$
S_F[\psi, \bar{\psi}] = a^4\sum_{n\in\Lambda}\bar{\psi}(x)M_{xy}[U]\psi(y) \tag{2.24}
$$

with

$$
M_{xy}[U] = \sum_{\mu=1}^{4}\gamma_\mu\frac{U_\mu(x)\delta_{x,(y-\hat{\mu})} - U_{-\mu}^\dagger(x)\delta_{x,(y+\hat{\mu})}}{2a} + m\delta_{x,y} \tag{2.25}
$$

in momentum space the propagator becomes:

$$\tilde{M}_{pq} = \delta(p-q)\tilde{M}(p) \quad \text{where} \quad \tilde{M}(p) = m\mathbb{1} + \frac{i}{a}\sum_{\mu=1}^{4}\gamma_\mu \sin(p_\mu a) \tag{2.26}$$

In order to calculate the inverse of the propagator in real space we need to invert the one in momentum space and perform an inverse Fourier transform. However, the inverse of the propagator in Fourier space has multiple poles, for example in the case of massless fermions:

$$\tilde{M}(p)^{-1}\Big|_{m=0} = \frac{-ia\sum_\mu \gamma_\mu \sin(p_\mu a)}{\sum_\mu \sin^2(p_\mu a)} \tag{2.27}$$

the problem vanishes for $a \to 0$, the continuum case, returning just one fermion type, but on the lattice multiple fermions, one for each pole emerge. This is known as the "doubling problem" and the extra fermions are called doublers. The solution, proposed by Wilson [10], is to modify the propagator adding a term that makes the poles in the inverse of the Fourier transformed propagator vanish. In momentum space:

$$M^W(p) = m\mathbb{1} + \frac{i}{a}\sum_{\mu=1}^{4}\gamma_\mu \sin(p_\mu a) + \mathbb{1}\frac{1}{a}\sum_{\mu=1}^{4}(1-\cos(p_\mu a)) \tag{2.28}$$

and in coordinate space:

$$M^W_{xy}[U] = \frac{1}{2a}\sum_{\mu=\pm1}^{\pm4}(\mathbb{1}-\gamma_\mu)U_\mu(x)\delta_{x,(y-\hat{\mu})} + \left(m + \frac{4}{a}\right)\delta_{x,y} \tag{2.29}$$

the shorthand notation $\gamma_{-\mu} = -\gamma_\mu$ has been introduced.
The final form of the Wilson Fermion Action is:

$$S_F[\psi,\bar{\psi}] = a^4 \sum_{n\in\Lambda} \bar{\psi}(x) M^W_{xy}[U]\psi(y) \tag{2.30}$$

Now that all the needed information about the action and the fields is set, mainly through equations 2.23 and 2.30, the picture of how to discretize QCD from the continuum Minkovskian space-time to an euclidean space-time lattice is complete.

2.3 Path Integrals on the Lattice

To express expectation values and correlators on the lattice, path integral formalism is used. The partition function, as we have seen earlier, is the path integral of the fields over the whole space of the action. For the case of QCD the fields are U, ψ and $\bar{\psi}$:

$$Z = \int \mathcal{D}\psi\mathcal{D}\bar{\psi}\mathcal{D}U e^{-S[\psi,\bar{\psi},U]} \tag{2.31}$$

with the action being the sum of the gluonic and fermionic parts:

$$S[\psi,\bar{\psi},U] = S_G[U] + S_F[\psi,\bar{\psi},U] = S_G[U] + \sum_f \bar{\psi} M[U]\psi \tag{2.32}$$

The immediate simplification is to integrate out the fermion fields. As in the continuum case one can perform an integration on the Grassmann-valued fields, in general for an integral over some Grassmann numbers θ_i and their complex conjugates θ_i^*, and a Hermitean matrix K:

$$\begin{aligned}\int \mathcal{D}\Theta^* \mathcal{D}\Theta e^{-\Theta K \Theta} &= \left(\prod_i \int d\theta_i^* d\theta_i\right) e^{-\theta_i^* K_{ij}\theta_j} = \left(\prod_i \int d\theta_i^* d\theta_i\right) e^{-\sum_i \theta_i^* k_i \theta_i} \\ &= \prod_i b_i = \det B\end{aligned} \tag{2.33}$$

This result is very different from what one would get in the real case, $(2\pi)^n / \det B$. It can also be shown that:

$$\begin{aligned}\int \mathcal{D}\Theta^* \mathcal{D}\Theta \theta_a^* \theta_b e^{-\Theta * K \Theta} &= \left(\prod_i \int d\theta_i^* d\theta_i\right) \theta_a^* \theta_b e^{-\theta_i^* K_{ij}\theta_j} = \left(\prod_i \int d\theta_i^* d\theta_i\right) \theta_a^* \theta_b e^{-\sum_i \theta_i^* k_i \theta_i} \\ &= (\det B)(B^{-1})_{ab}\end{aligned} \tag{2.34}$$

This last result is crucial for computing fermion correlators for example, for a given "source" $\bar{\psi}(x)$ and a "sink" $\psi(y)$ the propagator between the two can be computed via path integrals, but it requires inverting the fermion action matrix.
With the result of 2.33 we can simplify greatly the partition function:

$$Z = \int \mathcal{D}\psi \mathcal{D}\bar{\psi} \mathcal{D}U e^{-S[\psi,\bar{\psi},U]} = \int \mathcal{D}U e^{-S_G[U]} \det M[U] \tag{2.35}$$

In a similar fashion as in statistical mechanics, the expectation value of an observable on the lattice can be computed, recalling the general form eq. (2.2) as:

$$\langle O \rangle = \frac{1}{Z} \int \mathcal{D}U \; O[\psi,\bar{\psi},U] e^{-S_G[U]} \det M[U] \tag{2.36}$$

The above expression cannot be evaluated or simplified analytically any further, so the usual approach is to approximate the path integral numerically. The main idea is to create an ensemble of field configurations using the probability distribution:

$$P[U] = \frac{e^{-S_G[U]} \det M}{Z} \tag{2.37}$$

To reproduce the integral in eq. (2.36), on such set $\mathcal{U} = \{U_1, U_2, \ldots, U_N\}$ of configurations one computes the observable, the average value is the expectation value:

$$\langle O \rangle = \int \mathcal{D}U \; P[U] O[\psi,\bar{\psi},U] \approx \frac{1}{N} \sum_{i=1}^{N} O(\psi,\bar{\psi},U_i) \tag{2.38}$$

The choice of the set $\mathcal{U}$ is the interesting, but difficult, part which is solved by using Monte Carlo methods. The different configurations are chosen in the most widely accepted solution via a Markov chain. In chapter 4 a more detailed description of this problem, and a sketch of the implementation that has been developed, will be presented.

2.3.1 Pure Gauge Field Theory

Computing full QCD on the lattice is computationally expensive, mainly due to the integration of fermions via the determinant. From a numerical point of view, the determinant need to be computed at every step of the Markov chain that is used to evaluate the path-integral and this operation affects the time cost of sampling the configuration space dramatically. A first approach is to neglect the determinant completely, considering it constant. This is effectively removing dynamical fermions, freezing them to the lattice sites. This approximation is usually referred to as "quenched QCD", or QQCD.
The properties of this theory, that is then reduced to a simple Yang-Mills theory with zero fermion flavors, are still interesting to study and have historically played a very important role, being the only accessible simulation until sufficient computing power became available. For example, from eq. (1.19) one can see that the theory presents confinement and asymptotic freedom.

2.3.2 Observables

On the lattice, given the transformation 2.12, any product of link variables that starts and end at the same site, a closed loop, is gauge invariant. The average values of these objects over the whole lattice can be linked to physical observables, for example the field tensor. In a more general form any observable $L[U]$ of the type:

$$L[U] = \mathrm{Tr}\left[\prod_{(n,\mu)\in\mathcal{P}} U_\mu(n)\right] \tag{2.39}$$

where $\mathcal{P}$ is a closed path of links on the lattice, is a gauge invariant object.

Plaquette

The simplest observable, which we have already encountered upon defining the Wilson action in 2.23, is the plaquette. This is the minimal closed loop on the lattice and its value is related to the coupling constant of the action. For each lattice site there are 12 possible plaquettes to be computed, given all the combinations of euclidean indeces. One can consider the average value of the plaquette on the lattice as an observable, related to the value of the action of the field. A proper definition of the observable is:

$$P[U] = \frac{1}{6V}\sum_{n\in\Lambda}\sum_{\mu<\nu} P_{\mu\nu}(n) \tag{2.40}$$

where $P_{\mu\nu}(n)$ is the one defined in eq. (2.18) and V is the number of dimensionless lattice volume (the total number of lattice sites).
The plaquette expectation value can be used as a tool to determine when the Markov Chain that is used to generate the ensemble, to measure other observables, has reached a stationary point of the action. In particular, in section 5.2.1, the use of the plaquette for checking thermalization of the chain is discussed.

Energy Density

The energy of the field is proportional to the square of the field tensor, so the energy density is in particular:

$$E[U] = -\frac{1}{4V}\sum_{n\in\Lambda}\sum_{\mu<\nu}\mathrm{ReTr}(G_{\mu\nu}G^{\mu\nu}) \tag{2.41}$$

In order to estimate this quantity, one has to compute the field tensor at every lattice site, square it and sum over the whole space. It is then usually normalized by the lattice volume (the number of sites), to get the density. The simplest definition of the field tensor is $G^{(plaq)}_{\mu\nu} = \mathbb{1} - P_{\mu\nu}$ but this is not very accurate. A more symmetric definition can be obtained by the "clover" field tensor, that is the sum of all the plaquettes of a same plane $\mu\nu$ that start from a given lattice site take all with the same orientation.

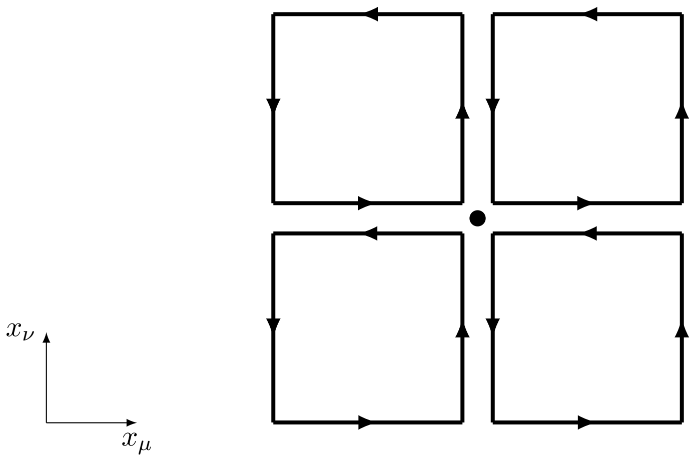

Figure 2.3: Schematic representation of the symmetric definition of the clover term $G^{(clover)}_{\mu\nu}$ on the lattice.

In terms of link variables this is equal to:

$$\begin{aligned} G^{(clover)}_{\mu\nu}(n) = \frac{1}{4}\Big[& U_\mu(n)U_\nu(n+\hat{\mu})U^\dagger_\mu(n+\hat{\nu})U^\dagger_\nu(n) \\ & -U_\nu(n)U^\dagger_\mu(n+\hat{\nu})U^\dagger_\nu(n-\hat{\mu})U_\mu(n-\hat{\mu}) \\ & +U^\dagger_\mu(n-\hat{\mu})U^\dagger_\nu(n-\hat{\mu}-\hat{\nu})U_\mu(n-\hat{\mu}-\hat{\nu})U_\nu(n-\hat{\nu}) \\ & -U^\dagger_\nu(n-\hat{\nu})U_\mu(n-\hat{\nu})U_\nu(n+\hat{\mu}-\hat{\nu})U^\dagger_\mu(n)\Big] \end{aligned} \tag{2.42}$$

Topological Charge

The gauge fields in QCD exhibit particular topological properties that are believed to have important physical implications [13][14]. The topological charge is an integer quantum number of the field in the continuum, similar to the concept of winding-number. In general fields with different topological charge are separated, but there exist non-zero instanton modes [15] that allow tunneling between them. On the lattice certain definitions can be used to reproduce the continuum properties, especially for the so called "topological susceptibility", that is the second moment of the distribution of the topological charge, which seems to be independent from the definitions of the base observable [16][17].

The topological charge is the integral over all space-time of the topological charge density:

$$Q = \int d^4 x q(x) \tag{2.43}$$

where

$$q(x) = \frac{1}{64\pi^2} \mathrm{Tr}(G_{\mu\nu}\tilde{G}^{\mu\nu}) \tag{2.44}$$

with $\tilde{G}^{\mu\nu} = \frac{1}{2}\epsilon^{\mu\nu\rho\sigma}G^{\rho\sigma}$. This can be estimated on the lattice, in the simplest way, by using the same definition of the field strength tensor we used before for the energy density, the clover:

$$Q[U] = \frac{1}{64\pi^2} \sum_{n\in\Lambda} \sum_{\mu<\nu} \epsilon^{\mu\nu\rho\sigma} \mathrm{Tr}[G^{(clover)}_{\mu\nu}(n) G^{(clover)}_{\rho\sigma}(n)] \tag{2.45}$$

As the lattice spacing is reduced, approaching the continuum, the topological sectors get more and more separated, preventing tunneling between them. This makes the Markov chain used to generate the ensemble less efficient in terms of growing autocorrelation times, as will be shown in section 5.2.
A derived quantity of great interest is the topological susceptibility χ, that is proportional to the expectation value of the square of the topological charge:

$$\chi = \frac{(\hbar c)^4}{a^4 |\Lambda|} \langle Q^2 \rangle \tag{2.46}$$

This observable is particularly important for the properties of instantons on the lattice and its value can be related via the Witten-Veneziano formula [13] to the mass of the η' meson, the pseudo-scalar singlet.

2.4 Modern Lattice QCD Calculations

motlo vaga...
The state of the art calculations in Lattice QCD involve improved fermion and gluon actions. For the gluon sector the improvements are based on finding linear combinations of gauge invariant loops, such as 2×1, 2×2 and 3×1 rectangles to systematically remove the higher order in the right-hand side of eq. (2.21). For fermions the improvements consist on actions that

preserve certain symmetries more than others, like chiral fermion actions or staggered fermions. On the algorithm side, the currently most used method to generate gauge field configuration is the Hybrid Monte Carlo method, which combines stochastic sampling with hamiltonian dynamic updates in the gauge field space. Other interesting algorithmic problems regard the calculation of fermion determinants, which typically involve very large sparse matrix diagonalization.
A fundamental concept in Lattice calculations is to recover the continuum limit in a controlled manner at the end of the analysis. The error sources that come into play when discretizing space-time on a fixed lattice are:

- Finite Volume Effects: caused by the non infinite domain of the simulation. Usually periodic boundary conditions are implemented to simulate infinite space, but one should always check if the total lattice volume is large enough, especially when dealing with large systems such as multiple baryons.
- State Isolation and Signal to Noise: when computing correlators between two points on the lattice it is possible to extract energy states of hadrons by looking at the exponential decay of the correlator in euclidean time. However this problem is largely affect by random noise making it hard to extract even the ground state most of the times; excited states are rarely considered.
- Chiral Limit: by which is intended the limit for which the masses of the quarks, and consequently of the computed hadrons, on the lattice approach the physical masses. One might question why this is even the case and that calculations should be performed at the physical masses only. However, the fermion propagator matrix becomes more and more sparse the lower he mass of the quark is, making the numerical algorithms that should diagonalize it slower to converge. The usual approach is to perform calculations on a set of pion masses (this is the usual reference for this problem) and afterwards the limit for $m_\pi^{(lat)} \to m_\pi^{(phys)}$ is taken to reproduce the physical observables.
- Continuum Limit: perhaps the most obvious thing to do to improve Lattice QCD calculations is to take finer and finer lattice spacings, to approach the continuum case. It should be noted however that this procedure has two downsides. First the lattice spacing in physical units is fixed by the quark masses, and as we previously mentioned, this affects the feasibility of the numerical simulation itself. Secondly, as the lattice approaches the continuum case the autocorrelation of observables in a given ensemble increases rapidly. This behavior, known as "critical slow-down" depends on the observable itself, some are more affected then others The integrated autocorrelation time for the topological charge for example is believed to have either power-law with a large exponent or even an exponential relation to the lattice spacing.

As one can notice, Lattice QCD is still an open field of research in many aspects: the algorithmic/numerical, the extraction and improvement of the measurement of physical quantities and the theoretical model itself.

Chapter 3

Advanced Topics in Lattice QCD

In this sections we will present some problems and methods that are used in Lattice QCD and in lattice Pure Gauge Theories. A 4-loop corrected expression for the β-function of QCD will be discussed as well, together with a tentative method of determining the scale parameter Λ from lattice calculations.

3.1 Scale Setting in the Quenched Approximation

On the lattice quantities are defined to be dimensionless and in order to link them with physical observables they need to be fixed by the correct power of the lattice spacing a to reproduce the physical units. The fundamental question is then how to connect the lattice spacing to the coupling used in the gluonic action. The general strategy is to compute on the lattice a quantity that is very well known in physical units.
In 1993 R. Sommer proposed to use the static quark potential as a reference in the case of $SU(2)$ theory [18]. Later in another work [19] a length scale r_0 was suggested for $SU(3)$ Yang-Mills theory to be set as the distance such that

$$r_0^2 F(r_0) = 1.65 \tag{3.1}$$

with $F(r_0)$ being the force between external static charges. In [19] also a parametrization of the ratio a/r_0 is provided, in terms of the coefficients of the renormalization group equation. To leading order one finds:

$$\frac{a}{r_0} \propto e^{-\frac{\beta}{12 b_0}} \tag{3.2}$$

with inverse coupling $\beta = 6/g_0^2$ and b_0 the one loop coefficient of the perturbative expansion of the β function, see section 1.2.1 , $b_0 = 11/(4\pi)^2$. Using the ansatz:

$$\ln\left(\frac{a}{r_0}\right) = \sum_{k=0}^{p} a_k (\beta - 6)^k \tag{3.3}$$

a parametrization up to $p = 3$ has been fitted to data. The resulting interpolating function is:

$$\ln\left(\frac{a}{r_0}\right) = -1.6805 - 1.7139(\beta - 6) + 0.8155(\beta - 6)^2 - 0.6667(\beta - 6)^3 \tag{3.4}$$

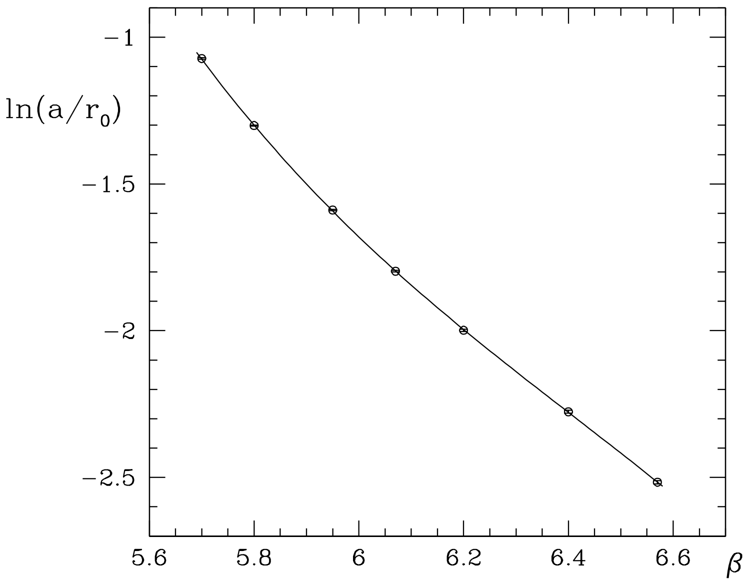

Figure 3.1: Data and interpolating function for $\ln(a/r_0)$ as found in [19].

This scale fixing procedure requires a proper estimate of the length scale from measurements of the static quark potential for various quark sources, which is an expensive calculation. Often it is custom to set the length scale to a fixed value, namely $r_0 = 0.5$ fm, commonly called the Sommer scale parameter, and then use eq. (3.4) to extract a.
More recently another procedure to fix the energy scale has been proposed, based on the Gradient Flow Method, which will be discussed in section 3.3.1. The key idea is again to choose and observable that is finite in the continuum limit, so lattice spacing independent. By fixing value for it one can use the quantity as a reference scale for further calculations.

3.2 The Gradient Flow Method

The Gradient Flow Method, also known as the Wilson Flow in the case of QCD, is a method for studying non-linear quantum field theories by the properties of flows in the field space. The key idea is to see how the theory evolves as it becomes less local, by driving it to the stationary points of the action, applying a "diffusion-like" differential equation to the field in a fictitious dimension called "flow time".
For the $SU(3)$ gauge field case most of the theoretical foundation was set by M.Lüscher in

[20][21] and for QCD in [22]. Starting from a field $A_\mu(x)$ the characterizing equations are:

$$\begin{aligned} &\partial_{t_f} B_\mu = D_\mu G_{\mu\nu} \\ &G_{\mu\nu} = \partial_\mu B_\nu - \partial_\nu B_\mu + [B_\mu, B_\nu] \\ &D_\mu = \partial_\mu + [B_\mu, \cdot\,] \end{aligned} \tag{3.5}$$

where the $B(t_f, x)$ field is the flowed version of the original field at flow time t_f. This is imposed by fixing:

$$B_\mu|_{t_f=0} = A_\mu \tag{3.6}$$

The second equation of eq. (3.5) is the generalization of the field strength tensor of the field B; the right-hand side of the first equation is then proportional to the gradient of the action. The effect of the gradient flow equations is to move the field along the direction of the minimum action, eventually reaching the stationary points. In a discretized theory taking the derivatives is not a trivial procedure, but we can use instead the intuitive idea of the flow equations, that is to use the steepest descent method on the action of a field. We then introduce the flowed lattice gauge field $V_{t_f}(x, \mu)$ as the flowed version of a field $U(x, \mu)$. Our flow equation then becomes:

$$\partial_{t_f} V_{t_f}(x, \mu) = -g_0^2[\partial_{x,\mu} S_G(V_{t_f})] V_{t_f}(x, \mu) \tag{3.7}$$

where S_G is the Wilson action, as defined in eq. (2.23), generalized to flowed fields. The generalization is really straightforward, as it only requires to compute the Wilson loops on the flowed gauge field.
The flow equations for the fermion fields, although they have not been used in this work, are:

$$\begin{aligned} &\partial_{t_f}\chi = \Delta\chi, \qquad &&\partial_{t_f}\bar{\chi} = \bar{\chi}\overleftarrow{\Delta} \\ &\Delta = D_\mu D_\mu, \qquad &&D_\mu = \partial_\mu + b_\mu \end{aligned} \tag{3.8}$$

note that Δ is the covariant laplacian in this notation. The initial conditions are naturally

$$\chi|_{t_f=0} = \psi, \qquad \bar{\chi}|_{t_f=0} = \bar{\psi}, \tag{3.9}$$

3.3 Perturbative Analysis of the Wilson Flow

An important thing to consider when applying the Wilson flow to a field is the renormalization of the observables: one has to check that expectation values of observables at non-zero flow time are renormalized quantities. Following the calculations performed in [20], we will consider the energy as our base observable.
First, we note that the flow equation is invariant under flow time independent gauge transformations, this prevents a detailed study of the renormalization. So we consider a modified version of the flow equation by adding one term:

$$\partial_{t_f} B_\mu = D_\mu G_{\mu\nu} + \lambda D_\mu \partial_\nu B_\nu \tag{3.10}$$

the original case is obtained again by setting $\lambda = 0$ and considering:

$$B_\mu = \Lambda B_\mu|_{\lambda=0}\Lambda^{-1} + \Lambda\partial_\mu\Lambda^{-1} \tag{3.11}$$

and with $\Lambda(t,x)$ now being a flow time dependent gauge transformation, set by:

$$\partial_{t_f}\Lambda_\mu = -\lambda\partial_\nu B_\nu \Lambda \quad \text{with} \quad \Lambda|_{t_f=0} = 1 \tag{3.12}$$

To leading order, and with the choice of $\lambda = 1$, it was shown in [21] that eq. (3.10) reduces to:

$$\partial_{t_f} B_\mu - \partial_\nu\partial_\nu B_\mu = 0 \tag{3.13}$$

which has a solution, in terms of the initial field $A_\mu(x)$ of the type:

$$B_\mu(t_f, x) = \int d^4y \frac{e^{-(x-y)^2/4t_f}}{(4\pi t_f)^2} A_\mu(y) \tag{3.14}$$

this result shows that the flow equations, as a first approximation, are a smearing operation. The right-hand side can be seen as the integral average of the original field weighted with a gaussian distribution of variance $2t_f$ and mean-square-radius of $\sqrt{8t_f}$.

The energy E as defined in eq. (2.41) is a gauge invariant object. One can observe that the modified flow equation is invariant under gauge transformations, hence the energy, as any other gauge invariant observable, will preserves its invariance. Using the modified flow equation it is possible to write the expectation value of the energy as a function of the flow time and of the renormalized coupling [20]:

$$\langle E\rangle = \frac{3(N^2-1)g_0^2}{128\pi^2 t_f^2}\left[1 + \bar{c}_1 g_0^2 + \mathcal{O}(g_0^4)\right] \tag{3.15}$$

with:

$$\bar{c}_1 = \frac{1}{16\pi^2}\left[N\left(\frac{11}{3}L + \frac{52}{9} - 3\ln 3\right) - N_f\left(\frac{2}{3}L + \frac{4}{9} - \frac{4}{3}\ln 2\right)\right] \tag{3.16}$$

The equation is for general N, the gauge group dimension, and number of quark flavors N_f. The coefficient $\bar{c}_1$ is in terms of a scale $L = \ln(8\mu^2 t_f) + \gamma_E$ where μ is the renormalization energy scale and γ_E Euler's constant. From this last relation we can set a flow energy scale as $q = 1/\sqrt{8t_f}$ and give a definition of eq. (3.15) in terms of the running coupling $\alpha_s(q) = \frac{g_0^2}{4\pi}$:

$$\langle E\rangle = \frac{3(N^2-1)}{32\pi t_f^2}\alpha_s(q)\left[1 + k_1\alpha_s(q) + \mathcal{O}(\alpha_s^2)\right] \tag{3.17}$$

where the coefficient k_1 is now:

$$k_1 = \frac{1}{4\pi}\left[N\left(\frac{11}{3}\gamma_E + \frac{52}{9} - 3\ln 3\right) - N_f\left(\frac{2}{3}\gamma_E + \frac{4}{9} - \frac{4}{3}\ln 2\right)\right] \tag{3.18}$$

In the case of $SU(3)$ symmetry group we have:

$$\langle E\rangle = \frac{3}{4\pi t_f^2}\alpha_s(q)\left[1 + k_1\alpha_s(q) + \mathcal{O}(\alpha_s^2)\right], \qquad k_1 = 1.0978 + 0.0075 \times N_f \tag{3.19}$$

The perturbative expansion is only valid for large values of q, that is when the flow time is small. We also can notice that $\sqrt{8t_f}$ is the inverse of an energy, or a length. This gives us a further

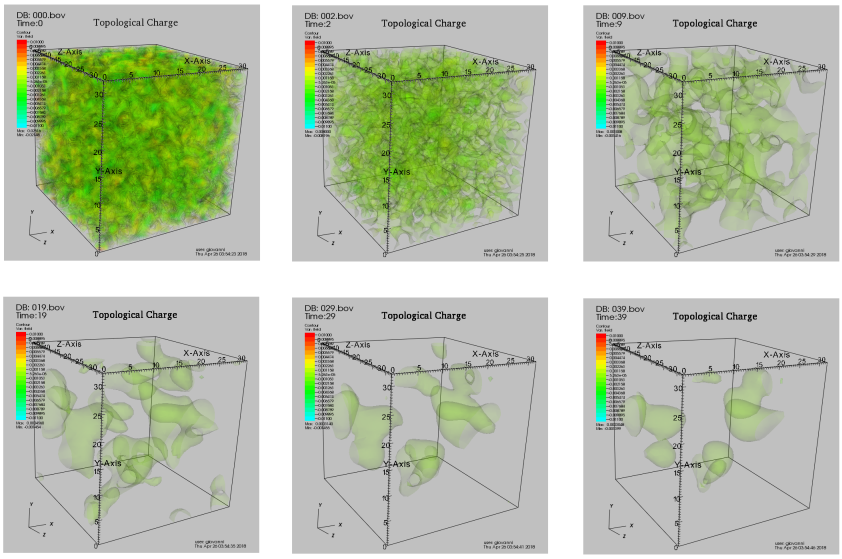

Figure 3.2: Topological charge computed ad one euclidean time of a lattice of size $32^3 \times 64$ with lattice spacing 0.06793 fm. The flow different plots are for flow times $\sqrt{8t_f} = 0, 0.14, 0.30$ fm on the first row and $\sqrt{8t_f} = 0.43, 0.52, 0.60$ fm on the second row. The visualization has been performed using a custom `python` interface, called “LatViz”, to the open source tool VisIt by LLNL [23]; developed together with H.M.Vege

intuitive picture of what the gradient flow equations do, that is to smear the field over a hypersphere of radius $\sqrt{8t_f}$. The gradient flow is particularly interesting to study quantities that are divergent on the lattice because of discretization effects, like the topological susceptibility, which become smooth at non-zero t_f. In fig. 3.2 an example of the smearing effect of the gradient flow on the topological charge. The topological charge at $\sqrt{8t_f} = 0$ is highly affected by large fluctuations over the lattice sites. This for example affects the topological susceptibility as it is divergent. One can notice that the action of the flow equation is to remove such low distance fluctuations that at $\sqrt{8t_f} = 0$ fm are almost completely gone. For larger smearing radii the emergence of frozen well separated topological sectors becomes visible.

3.3.1 Scale Fixing with the Gradient Flow

Because of the smearing properties of the flow equation the fields are driven towards the minima of the action, which are in general independent from the lattice spacing. One can therefore set, for sufficiently large flow times, decide to use the value of the dimensionless quantity $t^2\langle E\rangle$ to fix the scale of the lattice.
It has been proposed by Lüscher that a value of $t^2\langle E\rangle = 0.3$ is large enough to be used as a reference scale. In fig. 3.3 we can indeed observe that the value is constant as a function of the lattice spacing (computed instead using the Sommer parameter). In section 7.1 this method will be applied and discussed more thoroughly.

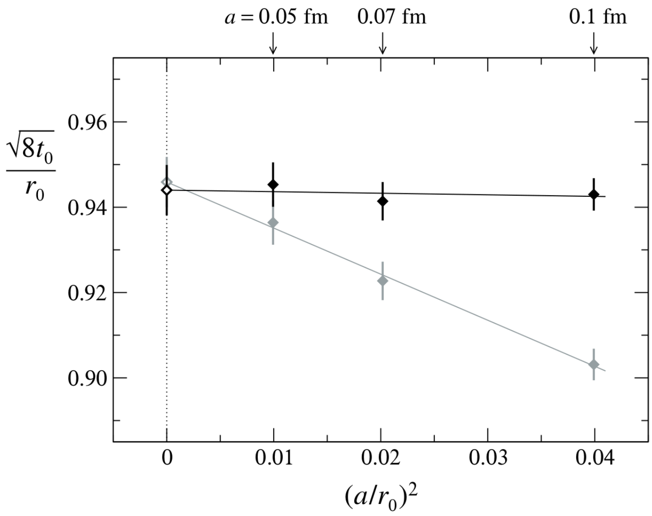

Figure 3.3: Plot of $\sqrt{8t_0}/r_0$ where t_0 is the value such that $t_0^2\langle E\rangle = 0.3$ for different lattice spacings taken from [24].

3.4 Estimating the Scale Parameter

Finally all the theoretical concepts and tools have been defined to state the main purpose of this work in a formal way. The goal is to use the perturbative expression of the energy as a function of the flow time and of the running coupling to estimate the momentum scale Λ. Since the algorithm for generating gauge field configurations that has been developed only for pure gauge theory, we will restrict the analysis for $N_f = 0$ for now, but in a future work the more interesting determination of Λ_{QCD} could be performed the same way.
On the lattice the quantity $t_f^2\langle E\rangle$ can be computed easily, this leaves only the coupling on the right hand side of eq. (3.19) as the unknown variable. One can then choose an order for the expansion of the Renormalization Group Equation:

$$\mu^2 \frac{d\alpha(\mu)}{d\mu^2} = \beta(\alpha) = -(b_0\alpha^2 + b_1\alpha^3 + \dots) \tag{3.20}$$

When solving the equation for $\alpha(\mu)$ there is some freedom on the choice of the renormalization point, as we have seen in eq. (1.20), such that the equation in the end can be simplified by the introduction of a momentum scale.
Using the data computed on the lattice, by first taking the continuum limit in order to account for discretization effects, we want to estimate the momentum scale.

3.4.1 4-loop Corrected Running Coupling

The equation eq. (3.19) needs to be have a functional form for $\alpha(\mu)$ as input, here we report an expression that is including diagrams up to 4-loops in the calculations of the RGE, parametrized by 4 coefficients. The equation was taken by the Particle Data Group review of QCD[25]:

$$\alpha(\mu) = \frac{1}{b_0 t}\Bigg[1 - \frac{b_1 \ln t}{b_0 t} + \frac{b_1^2(\ln^2 t - \ln t - 1) + b_0 b_2}{b_0^4 t^2} \\ - \frac{b_1^3(\ln^3 t - \frac{5}{2}\ln^2 t - 2\ln t + \frac{1}{2}) + 3b_0 b_1 b_2 \ln t - \frac{1}{2}b_0^2 b_3}{b_0^6 t^3}\Bigg] \tag{3.21}$$

here the convenient notation of $t \equiv \ln \frac{\mu^2}{\Lambda^2}$ has been introduced. The coefficients b_0, b_1, b_2 and b_3 can be computed analytically for a general theory on $SU(3)$ with N_f quark flavors. While b_0 and b_1 have known exact values, the other two parameters are renormalization scheme dependent, and we chose the ones computed in the $\overline{MS}$ found in [26]. The coefficients are then:

$$\begin{aligned} b_0 &= \frac{1}{(4\pi)}\left[11 - \frac{2}{3}N_f\right] \\ b_1 &= \frac{1}{(4\pi)^2}\left[102 - \frac{38}{3}N_f\right] \\ b_2 &= \frac{1}{(4\pi)^3}\left[\frac{2857}{2} - \frac{5033}{18}N_f + \frac{325}{54}N_f^2\right] \\ b_3 &= \frac{1}{(4\pi)^4}\Bigg[\left(\frac{149753}{6} + 3564\zeta_3\right) - \left(\frac{1078361}{162} + \frac{6508}{27}\zeta_3\right)N_f \\ &\quad + \left(\frac{50065}{162} + \frac{6472}{81}\zeta_3\right)N_f^2 + \frac{1093}{729}N_f^3\Bigg] \end{aligned} \tag{3.22}$$

or in a numerical form, substituting also the Riemann zeta-function value $\zeta_3 = 1.202056903\ldots$ one gets the more handy expression

$$\begin{aligned} b_0 &\approx \frac{1}{(4\pi)}(11 - 0.66667N_f) \\ b_1 &\approx \frac{1}{(4\pi)^2}(102 - 12.6667N_f) \\ b_2 &\approx \frac{1}{(4\pi)^3}(1428.50 - 279.611N_f + 6.01852N_f^2) \\ b_3 &\approx \frac{1}{(4\pi)^4}(29243.0 - 6946.30N_f + 405.089N_f^2 + 1.49931N_f^3) \end{aligned} \tag{3.23}$$

with the aid of these coefficients the only unknown variable in eq. (3.22) is the momentum scale, so by fitting this function to the lattice over a range of energies where some degree of overlap is found can lead to an estimation of Λ.

Part II

Implementation

Chapter 4

Designing a Lattice $SU(3)$ Yang-Mills Theory Code

One of the major focuses of this work has been a completely new implementation of a program to generate and analyse $SU(3)$ lattice gauge field configurations. As it is common practice in Lattice QCD numerical implementations, the program is split in three parts:

1. *Generation of Gauge Fields*: in this case it is done using an implementation of the Metropolis algorithm using the gluonic Wilson action;

2. *Computation of Lattice Observables*: this includes applying the gradient flow to the gauge fields, as well as computing the energy density and the topological charge at every flow time; in other applications the computation of quark propagators and two- or three-point correlators are performed;

3. *Computation of Derived Quantities*: mainly post analysis, computation of secondary observables and uncertainties. Resampling and autocorrelation analysis are crucial to Lattice QCD given the typically small size of the ensembles.

In this chapter the main features of the first two steps, which are the most interesting, will be presented. The first two points are numerically very challenging and the calculations had to be performed on computing clusters. The third, the post analysis, is a simpler calculation, so regular tabletop computers could be exploited.
The programming language of choice was `C++` because of its high efficiency, high abstraction capabilities (the code-base is highly object oriented and extensive use of operator overloading was involved) and for the easiness of the `MPI` integration. The analysis of data has been performed using `python` and in particular relying heavily on its standard data science packages such as `numpy` and `pandas`.

4.1 Generating Pure Gauge Fields

The task of generating lattice field configurations is extremely demanding in terms of computation requirements. The case of QCD is much more demanding than that of a pure gauge theory, but overall the latter calculation is still challenging. The main, and perhaps overwhelmingly simple, reason for this problem is the dimensionality. Dealing with a discretized space-time lattice, things tend to scale with powers of 2^4, a trivial example is cutting in half the lattice spacing keeping a fixed total volume: this requires 16 more points in the global lattice.
To get a better feeling of the algorithm we first have to look at what the basic object of the program is: the lattice. On a computer the number of double precision floating point numbers to be stored for a field configuration is given by

$$\underbrace{N^3}_{\text{spatial dimension}} \times \underbrace{N_t}_{\text{time dimension}} \times \underbrace{4}_{\text{links per site}} \times \underbrace{9}_{\text{SU(3) matrix size}} \times \underbrace{2}_{\text{real and imaginary part}} \tag{4.1}$$

For example, if we choose $N = 48$, $N_t = 96$ (which is the largest system considered in this work) the resulting configuration is 6115295232 *bytes* large, that is 5.7 *GBytes*. The incredibly large size of the data to be handled limits greatly the possibility of simulating larger systems.
The basic element at each lattice site is a set of 4 different $SU(3)$ matrices, one for each dimension, these are the links variables described in section 2.2. Since the links with negative orientation are related to the ones with positive orientation by the adjoint operation, only the postively oriented ones are stored in memory.

4.1.1 The Metropolis Algorithm

The main algorithm that has been used to generate an ensemble of gauge field configurations is the Metropolis Algorithm. It is a widely popular Markov Chain Monte Carlo Method to generate a sequence of random samples from a probability distribution [27][28].
In general, a Markov Chain is a a sequence randomly chosen variables $X_1, X_2, \ldots, X_t$, in our case a lattice field configuration, with the Markov Property, that is: the probability of the step $t + 1$ depends only on the variable X_t:

$$P(X_{t+1} = x|X_1 = x_1, X_1 = x_2, \ldots, X_t = x_t) = P(X_{t+1} = x|X_t = x_t) \tag{4.2}$$

In the case where the probabilities of moving from a state $X_i = i$ to a state $X_j = j$ is not known, the transition probability from the two states, $W(i \to j)$ can be split into two contributions: the probability $T(i \to j)$ for making the transition to state j being in state i and the the probability of accepting this transition $A(i \to j)$.

$$W(i \to j) = A(i \to j)T(i \to j) \tag{4.3}$$

If a Probability Distribution Function (PDF) is known for the process, we can label the probability of a given state at a fixed time $w_i(t)$. The transition probability to a state j at time $t+1$ is the sum of the transition probabilities of moving to state j from state i plus the probability of being in state i at time t and rejecting to move to any other state:

$$\begin{aligned} w_j(t+1) &= \sum_i \left[w_i(t)T(i \to j)A(i \to j) + w_j(t)T(j \to i)\left(1 - A(j \to i)\right)\right] \\ &= w_j(t) + \sum_i \left[w_i(t)T(i \to j)A(i \to j) - w_j(t)T(j \to i)A(j \to i)\right] \end{aligned} \tag{4.4}$$

for large t, when the equilibrium is reached, we require that $w_j(t+1) = w_j(t) = w_j$, and thus we have:

$$\sum_i w_i T(i \to j)A(i \to j) = \sum_i w_j T(j \to i)A(j \to i) \tag{4.5}$$

now, considering that the transition probability from a state j to all other states must be normalized $\sum_i W(j \to i) = \sum_i T(j \to i)A(j \to i) = 1$ we get:

$$\sum_i w_i T(i \to j)A(i \to j) = w_j \tag{4.6}$$

At this point, the further constrain of Detailed Balance is introduced, that is:

$$w_i W(i \to j) = w_j W(j \to i) \tag{4.7}$$

at equilibrium we then have:

$$\frac{w_i}{w_j} = \frac{W(i \to j)}{W(j \to i)} = \frac{T(i \to j)A(i \to j)}{T(j \to i)A(j \to i)} \tag{4.8}$$

Making the approximation that the transition probability between states is the same, $T(i \to j) = T(j \to i)$, the brute-force approach, we are left with the acceptance ratio of a move to an new state to be the ratio of the PDFs.

In the case of pure gauge fields, the probability distribution is:

$$P(U) = \frac{e^{S_G[U]}}{Z} = \frac{e^{S_G[U]}}{\int \mathcal{D}\ U e^{S_G[U]}} \tag{4.9}$$

which is the exponential of gluon Wilson Action over the path integral of the same quantity over all space (the partition function). Luckily, we only need ratios of PDFs so the partition functions is not to be computed. We can rewrite any expectation value of an operator on the lattice as:

$$\langle O \rangle = \frac{\int \mathcal{D}U\ O[U] e^{S_G[U]}}{\int \mathcal{D}\ U e^{S_G[U]}} = \int \mathcal{D}U\ P(U)O[U] \tag{4.10}$$

which numerically becomes:

$$\langle O \rangle \approx \frac{1}{N} \sum_{i=1}^{N} O(U_i) \tag{4.11}$$

where, as described in section section 2.3 U_i are random configurations of a set chosen with the PDF in eq. (4.9).
Noting that, since we only care about ratios in the PDF, which turn out to be exponentials of the action difference between to configurations, a tentative algorithm can be written as:

Algorithm 1 Metropolis Algorithm

$configuration \leftarrow$ initial configuration
for $i < MonteCarloCycles$ **do**
  for $j < N_{corr}$ **do**
    for U in $Lattice$ **do**
      $newConfiguration \leftarrow \text{randomMove}(U) + configuration$
      $\Delta S \leftarrow \text{action}(newConfiguration) - \text{action}(configuration)$
      if $\Delta S > random(0, 1)$ **then**
        $configuration \leftarrow newConfiguration$
      end if
    end for
  end for
  saveConfiguration($configuration$)
end for

The actual implementation of this algorithm on discretized space-time is however not as trivial as it seems. Firstly, a definition of what is a "random move" in configuration space is needed, secondly an efficient way of computing the action difference is to be found.

The ensemble, on which observables can be computed, is created by saving to disk, in the form of a simple binary file containing all the data, one configuration every N_C Monte Carlo updates. We need this in order to apply the gradient flow afterwards to the configurations and compute the observables we want. The choice of N_C turned out to be crucial for the autocorrelation of some observables, in particular the topological charge, see section 5.2.

4.1.2 Sampling the Configuration Space

To use Metropolis' algorithm we need to define what a random move is. Using the Wilson Action eq. (2.13), which is defined on plaquettes, an random move in the configuration space, on a single link variable, can be seen as a small unitary transformation in the $SU(3)$ group. By small it is intended that the unitary matrix has a strong real diagonal component, making it close to an identity matrix. In order to generate such transformation we use three random $SU(2)$ matrices that are as well "close to unity". A recipe for generating these matrices is found in [11]. We consider three 2×2 unitary matrixes R_2, S_2 and T_2:

$$R_2 = \begin{pmatrix} r_{11} & r_{12} \\ r_{21} & r_{22} \end{pmatrix} \qquad S_2 = \begin{pmatrix} s_{11} & s_{12} \\ s_{21} & s_{22} \end{pmatrix} \qquad T_2 = \begin{pmatrix} t_{11} & t_{12} \\ t_{21} & t_{22} \end{pmatrix} \tag{4.12}$$

The elements of the matrix are to be random but with a controlled spread around the identity matrix. One starts by selecting four random numbers r_0, $\mathbf{r}$ (the latter is a three component vector) between $(-\frac{1}{2}, \frac{1}{2})$. Then a "spread parameter" ϵ is introduced, which controls how much the off-diagonal terms will weight. The random variables are scaled according to:

$$x_0 = sign(r_0)\sqrt{1-\epsilon^2} \qquad \mathbf{x} = \epsilon\frac{\mathbf{r}}{|\mathbf{r}|} \tag{4.13}$$

and these four coefficients, together with the generators of the $SU(2)$ group (the Pauli matrices) are used to build the element of the group:

$$U = x_0 \mathbb{1} + i\mathbf{x} \cdot \sigma = \begin{pmatrix} u_{11} & u_{12} \\ u_{21} & u_{22} \end{pmatrix} \tag{4.14}$$

One then embeds these $SU(2)$ matrices in three $SU(3)$ matrices by mapping them as:

$$R = \begin{pmatrix} r_{11} & r_{12} & 0 \\ r_{21} & r_{22} & 0 \\ 0 & 0 & 1 \end{pmatrix} \qquad S = \begin{pmatrix} s_{11} & 0 & s_{12} \\ 0 & 1 & 0 \\ s_{21} & 0 & s_{22} \end{pmatrix} \qquad T = \begin{pmatrix} 1 & 0 & 0 \\ 0 & t_{11} & t_{12} \\ 0 & t_{21} & t_{22} \end{pmatrix} \tag{4.15}$$

These three matrices are clearly members of the $SU(3)$ group and so is their product $X = RST$, which is used as the "random move" in the Metropolis algorithm. We thus have defined a recipe for numerically generating random transformations, the key element for our algorithm.

4.1.3 Efficient Action Difference Calculation

An additional element that is needed is the action difference ΔS. When a random transformation $U_\mu(x) \to U'_\mu(x) = XU_\mu(x)$ is applied on a single link of the lattice, the total change in the action only depends on those plaquettes that contain the considered link variable. In four dimensions there are 12 such elements:

$$\Delta S = S[U'_\mu(x)] - S[U_\mu(x)] = -\frac{\beta}{N} \text{Re } Tr \left([U'_\mu(x) - U_\mu(x)] A[U_\mu(x)] \right) \tag{4.16}$$

where $A[U_\mu(x)]$ is the sum of the "staples" of the link $U_\mu(x)$. They are the constant three sides of the plaquettes that contain $U_\mu(x)$:

$$\begin{aligned} A[U_\mu(x)] = \sum_{\nu \neq \mu} \Big[& U_\nu(x+\mu) U_{-\mu}(x+\mu+\nu) U_{-\nu}(x+\nu) \\ & + U_{-\nu}(x+\mu) U_{-\mu}(x+\mu-\nu) U_\nu(x-\nu) \Big] \end{aligned} \tag{4.17}$$

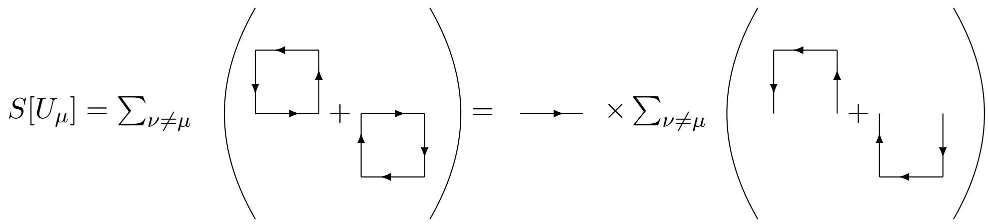

Figure 4.1: Schematic representation of the symmetric definition of action $S[U_\mu]$ expressed as a function of the staples .

Algorithm 2 Metropolis Update

for x, μ **do**
  $A \leftarrow computeStaples(x, \mu)$
  for $i < N_H$ **do**
    $U_{new}(x, \mu) \leftarrow X \cdot U(x, \mu)$
    $\Delta S \leftarrow (U_{new}(x, \mu) - U(x, \mu)) \cdot A$
    if $realTrace(\Delta S) > random(0, 1)$ **then**
      $U(x, \mu) \leftarrow U_{new}(x, \mu)$
    end if
  end for
end for

4.1.4 Updates Strategies

There is now some arbitrariness in what is defined as a Monte Carlo update, or cycle. In this work we call an update the procedure outlined in algorithm 2. These updates are the ones we consider when we refer to Monte Carlo cycles in the context of thermalization and autocorrelation time, for example. Note that each update includes a loop over all links on the lattice and that every link is "hit" N_H times before moving to the next one. This is done for computational efficiency, because computing the staples is the most expensive part of the algorithm, once A is computed for a link, the result is used to attempt multiple updates on the link. It can also be shown that if N_H is sufficiently large the algorithm becomes equivalent to the heatbath algorithm.

The order in which the links in the lattice are visited is also arbitrary. The simplest way, that is iterating on the links as they are stored in memory, was adopted. This however might have impacted the autocorrelation of the system, not allowing significant modification to the system as an update depends on the neighbors. An alternative choice is a checkerboard pattern, which has potential benefits to the autocorrelation time of the observables as well as on the performance, as it allows for better communication patterns in the case of parallelized code.

4.1.5 Parallelization Scheme

Given the size of the lattice (from $V \approx 10^5$ to $V \approx 10^7$, the total number of lattice sites), it is almost necessary to split the computation of the updates on more than one processors. The most direct way is to divide the lattice into sub-blocks and have each process handle its portion of the field alone.
In an operative way, given a lattice of size (n_x, n_y, n_z, n_t) each space-time dimension is split into even portions, of size (s_x, s_y, s_z, s_t) and mapped on N_{procs} processors, having that:

$$N_{procs} = \frac{s_x}{n_x} \times \frac{s_y}{n_y} \times \frac{s_z}{n_z} \times \frac{s_t}{n_t} \tag{4.18}$$

A unique mapping can be performed from the "local" coordinates of the sub-block and the global coordinates through the aid of the unique identifier of the processor that is given by the

parallelization library. In particular, the Message Passing Interface (MPI) has a built-in function to map processors into a grid of arbitrary dimensions and size, called `MPI_CartCoord_Create`. The utility also allows for the ease identification of the rank (the jargon term for the unique identifier of a processor) of the nearest neighbors. Using this tools one can manage the distribution of the total lattice into N_{procs} sub-lattices.
However, because of the dependence of the action difference of a link on its neighboring site, when updating a link on the edge of of a sub-block information about another block is needed. Here is where MPI comes in use, substituting the usual periodic boundary conditions that are used in the calculations with periodic communication patterns between the processors. For this particular problem we decided to use a point to point communication scheme, the use of periodic boundary conditions allowed also for non-blocking communications, in particular the collective geometry based scheme shown in section 4.1.5 has been implemented.

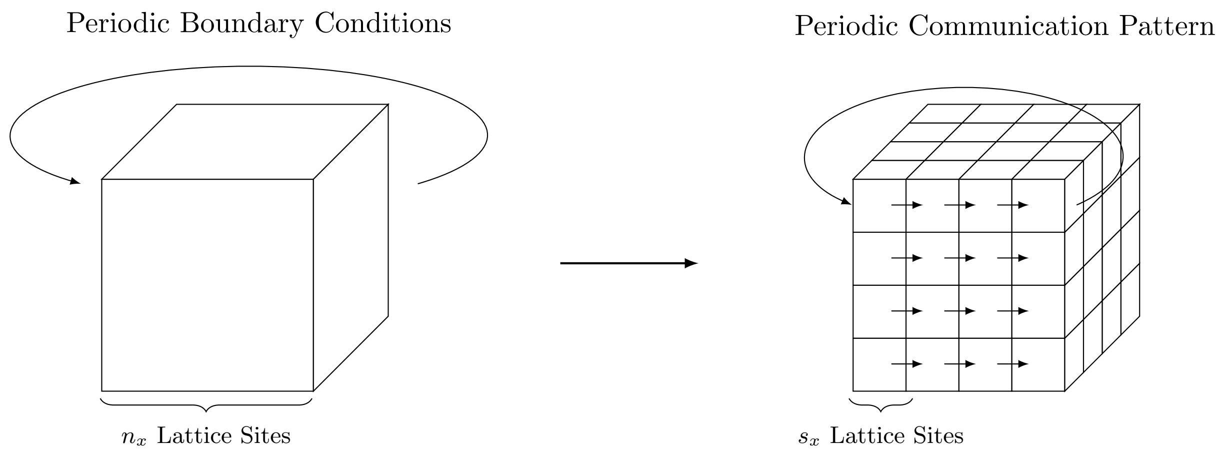

Figure 4.2: Schematic representation, in just 3 dimesnions, of the splitting of the lattice into sub-lattices.

When computing the staples, two links need to be fetched from the neighboring sites FIGURE? , since all processors are synchronized, when one processor is in need of these link variables one of its neighbors is requesting the corresponding links from it. The `SendRecv` function of MPI is exactly what is needed: it automatically handles, in the most efficient way, multiple data transfer between processors in situations when a single core needs to send and receive from different ranks.
Note that the communication is relevant only for the computation of the staples, this is another argument in favor of performing multiple hits on a link at every update. It is clear to see that the algorithm can be affected by large communication overhead problems. If the sub-blocks are too small, then most of the time would be spent on sending and receiving links from the neighbors. This causes the execution time to depend not linearly on the number of processors, instead the relation flattens at some value given by the communication overhead.

4.1.6 Summary of the Parameters for Generating Configurations

In total the algorithm has four parameters as inputs. Of these, only one defines the physics of the system, the others have to be set and optimized in order to improve the acceptance ratio of the metropolis algorithm and the autocorrelation of the observables computed on the generated configurations.

Parameter	Description
β	Coupling parameter of the Wilson Action
ϵ	"Spread" of the random $SU(3)$ elements for the updates
N_C	Number of updates between one saved configuration (observable measurement)
N_H	Number of of "hits" per link at every update, with constant staple

Table 4.1: Parameters for the Monte Carlo generation of Yang-Mills gauge field configurations via the Metropolis Algorithm

4.2 Gradient Flow of Gauge Configurations

To study the flow time dependence of the observables a numeric implementation of eq. (3.7) is needed. The main challenge that this problem poses is how to numerically integrate the flow equation on the lattice, because it is important to preserve the $SU(3)$ Lie Group structure of the field through the numerical procedure. The problem is solved by using the so called Structure-Preserving Runge-Kutta Methods, in particular the Runge-Kutta Munthe-Kaas method that is designed to integrate first order ODE on a manifold [29, 30, 31]. In algorithm 3 the general scheme of the program to flow the gauge field configurations is outlined.

Algorithm 3 Gradient Flow

for *conf* in *ensemble* **do**
  conf $\leftarrow$readInputFile()
  for $t = 0,\ t_f < t_f^{MAX}$ **do**
    conf $\leftarrow$flowStep(*conf*) computeObservables(*conf*)
    $t_f \leftarrow t_f + \epsilon$
  end for
end for

The main idea is to loop over all the configurations in an ensemble and for each of them numerically integrate in steps of ϵ (a dimensionless small step parameter) from $t_f = 0$ to $t_f = t_f^{MAX}$. By using an explicit RK method, only one lattice is stored in memory at a time, and is updated at every iteration. At each step, the expectation values of all the desired observables are computed and their value stored to file for further analysis.

4.2.1 Numerical Integration of the Flow Equation

The problem of the gradient flow can be defined in more general terms as:

$$\dot{V}_t = Z(V_t)V_t \tag{4.19}$$

here V_t is an element of a Lie group $\mathcal{G}$ and $Z(V_t)$ is a function with values in the associated algebra $\mathfrak{g}$, in our case we have $Z(V_t) = -g_0^2\partial_\mu V(t_f)$. The general ansatz for the RK-MK method is to write the integration step, with ϵ the integration step, as:

$$V_{t+\epsilon} = \exp[\epsilon\Omega(V_t)]V_t \tag{4.20}$$

where $\Omega(V_t)$ is a linear combination of $Z(V_t + \epsilon c_i)$, with c_i the RK coefficients, and of their commutators. Following the suggestion of [20] and considering the analysis of [32] that suggests that, for a fixed step size, an integrator of third order is sufficient, the integration scheme that has been used is the one found in Lüscher's article:

$$\begin{aligned} W_0 &= V_t \\ W_1 &= \exp\left[\frac{1}{4}Z_0\right]W_0 \\ W_2 &= \exp\left[\frac{8}{9}Z_1 - \frac{17}{36}Z_0\right]W_1 \\ V_{t+\epsilon} &= \exp\left[\frac{3}{4}Z_2 - \frac{8}{9}Z_1 + \frac{17}{36}Z_0\right]W_2 \end{aligned} \tag{4.21}$$

where the shorthand notation $Z_i = i\epsilon Z(W_i)$ has been introduced. The choice of the coefficients for the Butcher's tableu of the RK method is made in order to satisfy the requirements for a third order RK integrator and to cancel the commutator terms in $\Omega(V_t)$ when expanding it with the Baker-Campbell-Husdorff formula.

What is then left to define are the derivative of the action at a given lattice site and the numerical exponentiation of a member of the $\mathfrak{su}(3)$ algebra, which returns an $SU(3)$ element.

4.2.2 The Action Derivative

The differential operator acting on an algebra-valued function $f(U)$ in a Lie group is defined, in terms of the generators t^a:

$$\partial^a_{\mu,x} f(U) = \frac{d}{ds} f(e^{sX}U)\bigg|_{s=0}, \qquad \text{with} \quad X(\mu,x) = t^a\delta_{x,y}\delta_{\mu,\nu} \tag{4.22}$$

In practice this operator leaves unchanged all the links except the one that is being derived. When considering the action in eq. (2.23) and recalling the definition of staples eq. (4.17) we have:

$$\partial^a_{\mu,x} S_G(U_\mu(x)) = -\frac{2}{g_0^2}\sum_{x\in\Lambda}\sum_{\mu\neq\nu}\mathrm{ReTr}(1 - P_{\mu\nu}) = -\frac{2}{g_0^2}\mathrm{ReTr}(t^a U_\mu(x)A[U_\mu(x)]) \tag{4.23}$$

Defining $\Omega_\mu(x) = U_\mu(x)A[U_\mu(x)]$ and summing over all generators one has:

$$g_0^2 \partial_{\mu,x} S_G(U_\mu(x)) = 2t^a \mathrm{ReTr}(t^a \Omega_\mu(x)) = t^a \mathrm{Tr}(t^a(\Omega_\mu(x) - \Omega_\mu^\dagger(x)) \tag{4.24}$$

Invoking now the fact that any 3×3 matrix can be expanded as $M = \frac{1}{3}\mathrm{Tr}M - 2t^a \mathrm{Tr}(t^a M)$, inverting this relation we get:

$$g_0^2 \partial_{\mu,x} S_G(U_\mu(x)) = \frac{1}{2}\left(\Omega_\mu(x) - \Omega_\mu^\dagger(x)\right) - \frac{1}{6}\mathrm{Tr}\left(\Omega_\mu(x) - \Omega_\mu^\dagger(x)\right) \tag{4.25}$$

that is our final expression for the action derivative. It should be noticed that computing this term is not anymore complex than computing the action difference for the gauge field configuration generation case, as in both cases the most complicated object to calculate on the lattice is the sum of the staples. We can notice as well that the derivative is always a traceless hermitean matrix, thus an element of $\mathfrak{su}(3)$ as expected.

4.2.3 Exponential of a $\mathfrak{su}(3)$ Element

The last thing to define from eq. (4.21) is how to exponentiate the action derivative. Following [33] we provide a numerical recipe for taking the exponential function of a traceless hermitean 3×3 matrix. The key idea is to use the Cayley-Hamilton theorem, that states that every matrix is a zero of its characteristic polynomial:

$$Q^3 - c_1 Q - c_0 \mathbb{1} = 0, \qquad \text{with } \ c_0 = \det Q = \frac{1}{3}(Q^3), \quad c_1 = \frac{1}{2}(Q^2) \tag{4.26}$$

The exponential of iQ can then be written as:

$$e^{iQ} = f_0 \mathbb{1} + f_1 Q + f_2 Q^2 \tag{4.27}$$

where the functions of the eigenvalues of Q, which in turn can be parameterized, because of the hermitianeity of Q in terms of c_0 and c_1. Labeling the eigenvalues of Q as q_1, q_2, q_3 and using the fact that the matrix is traceless they can be parametrized as:

$$q_1 = 2u \qquad q_2 = -u + w \qquad q_3 = -u - w \tag{4.28}$$

with:

$$u = \sqrt{\frac{1}{3}c_1}\cos\left(\frac{1}{3}\theta\right) \qquad w = \sqrt{c_1}\sin\left(\frac{1}{3}\theta\right) \qquad \theta = \arccos\left[\frac{c_0}{2}\left(\frac{3}{c_1}\right)^{3/2}\right] \tag{4.29}$$

As shown in [33] the coefficients f_i can be written as:

$$f_i = \frac{h_i}{9u^2 - w^2} \tag{4.30}$$

with:

$$h_0 = (u^2 - w^2)e^{2iu} + e^{-iu}\left[8u^2\cos(w) + 2iu(3u^2 + w^2)\frac{\sin(w)}{w}\right] \tag{4.31}$$
$$h_1 = 2ue^{2iu} - e^{-iu}\left[2u\cos(w) - i(3u^2 - w^2)\right]$$
$$h_2 = e^{2iu} - e^{-iu}\left[\cos(w) + 3iu\frac{\sin(w)}{w}\right]$$

This fairly complicated algorithm is the core of the gradient flow implementation, because fundamentally the integration of the flow equation is an altenated sequence of staples calculation and matrix exponentials.

4.2.4 Parallelization Scheme

Also this problem is very expensive in computational terms, so it is worth designing a parallelization scheme for it. The idea is still to split the lattice into sub-blocks as in section 4.1.5 and have each processor handle one of them. By looking at eq. (4.21) we see that all operations can be defined on a lattice-wise scale and that they all depend on one previous state of the field, not on an intermediate one as was the case for the generation of gauge fields. This allows us to define a “lattice shift” operation, that effectively creates an additional lattice that is the translation of the original along an axis. The huge advantage is that in order to perform this operation only one communication instance is needed (following the previous scheme in section 4.1.5), but the message is now a whole shared cube between two processors. A simple 2D representation of the shift operation is drawn in fig. 4.3

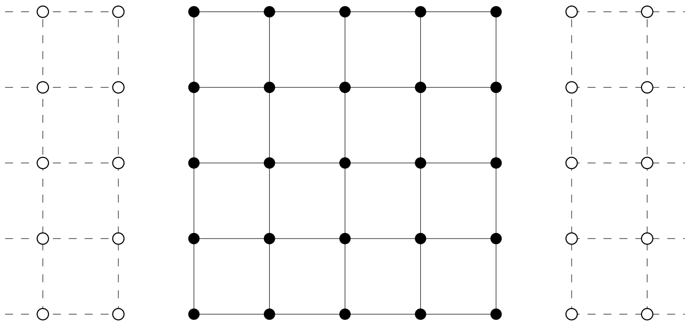

(a) Normally, one processor only has a local lattice and no data from the neighboring sub-lattices. An empty copy of the sub-lattice is made, to store the shifted lattice.

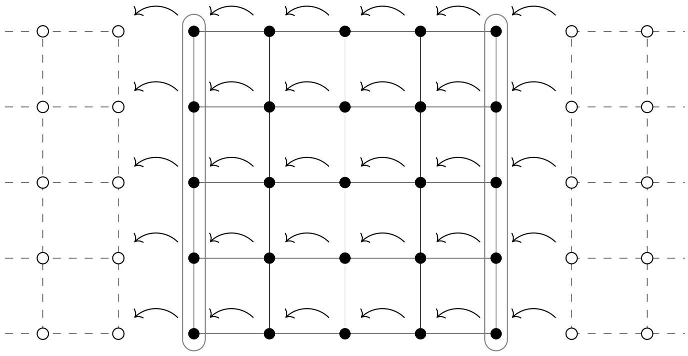

(b) The shifted lattice is filled with the neighboring links, some of which are received by the "forward" neighbor (so some are sent as well to the "backward" neighbor)

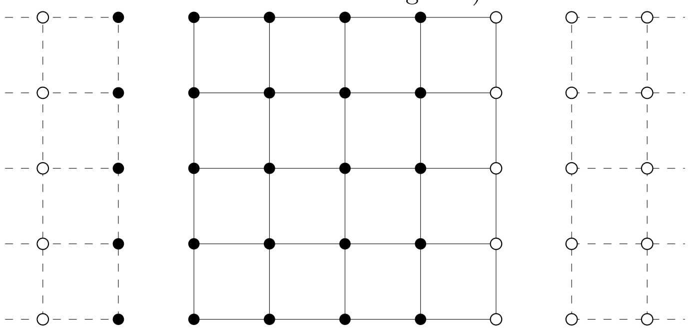

(c) The shifted lattice is now a local object mapped with the same indeces as the original one. A site-by-site multiplication is now possible between the original and the shifted lattices.

Figure 4.3: Parallelization scheme based on lattice shifts. When, for example in the staples computation, a link needs to be multiplied by a neighboring one, a new lattice is created. It is filled with the shifted link, which is fetched either from the local sub-lattice if it is in the central region, or from the neighbors if it is on the edge. This schematic drawing shows how a shift along the "right" direction is performed. A new lattice containing the data of the target link is created by filling it with the target links. The circled regions in fig. 4.3b, the edges, are shared using MPI by first creating a "buffer" of the shape of the edge (it is a cube in the real simulation) and it is sent in a single message to the neighbor which unpacks it in the right location. The new lattice is the multiplied with the original one on a site by site basis, which now is only a local operation.

The data to be shifted is on the order of hundreds of kilobytes, which takes some time to be sent by MPI. An optimization that has been implemented is then to rewrite the algorithm in order to use non-blocking communications, first instantiating a send instruction non-blockingly, then shifting the inner points of the sub-lattice (which do not require links from the neighbors), waiting for the message from the neighbor to arrive, receiving the data from the neighbor and placing it in the buffer space.
This lattice shift operation has been implemented for the action derivative lattice and the gauge field itself. The massive reduction in communication overhead, compared to the single link exchange in section 4.1.5, improved the scaling of the algorithm greatly, making this part of the problem much more efficient.

4.2.5 Summary of the Parameters for the Gradient Flow

As it has been done for the gauge field configuration generation algorithm, we report a summary of all free parameters of the program that performs the numerical integration of the gradient flow equation on the lattice configurations.

Parameter	Description
β	Coupling parameter of the Wilson Action, fixed by the input configuration
ϵ	Runge-Kutta integration step
t_f^{MAX}	Maximum value of the flow time reached for every configuration.

Table 4.2: Parameters for the numerical integration of the gradient flow equations on Yang-Mills gauge field configurations.

4.3 Structure and Tools

The full code can be found on the web under the link https://github.com/GioPede, where both the code for the generation and the flow of gauge fields are hosted. The technical documentation is found at https://giopede.github.io/LatticeYangMills/html/index.html and https://giopede.github.io/LatticeFlow/html/index.html. As already mentioned the language of choice was `C++`, mainly because of the high-performance and abstraction level it provides. An object-oriented structure has been used, as can be seen in

FIG: scheme class .

Notable tools that have been used that deserve a mention are `MPI` , nlhoman/json [34] (used for easy input parameters handling via json files), CMake (for building the project) and Valgrind for function and memory profiling.

Chapter 5

Tests and Runs Description

When developing a program for numerical simulations from scratch, it is crucial to design test cases and benchmarks to verify the goodness of the implementation. The easiest case is that of a fully deterministic program (for which the output depends only on some initial parameters) because one can compare the results with other implementations to validate the code. In the case of stochastic processes, like the Metropolis algorithm, it is only possible to compare the average behavior with external implementations.
In this chapter we will give an overview of the test cases, the properties of the ensembles used in this thesis and how the parameters that were needed to generate them have been set.

5.1 Generated Ensembles

In order to study the momentum scale it has been necessary to choose a set of decreasing lattice spacings to then be able to take the continuum limit. This procedure is common to most Lattice QCD calculations as it is the most straightforward way to take recover the continuum theory. The lattice spacing is linked to the coupling g_0 and β by the relation found in eq. (3.4).
We chose 4 values of β that span lattice spacings from approximately 0.1 fm to 0.05 fm in approximately equal steps.
For the calculation to be consistent however, the total volume of the lattice should be kept constant, so the choice of the lattice spacings also determined the number of lattice sites per dimension, having $L = aN \approx const$. The time dimension has been take to be twice as big as the space dimension. The number of lattice points per dimension, for parallelization's sake, were chosen in order to have many divisors, to allow for different and small sub-blocks.
Table section 5.1 summarizes the physical properties of the ensembles that were generated. For each value of β a statistical ensemble was needed. Ideally, one would take as many configurations as possible for each value and in principle one would have the same number of configurations for each of them. However it is clear from the discussion in chapter 4 that the number of lattice sites affects computation times and the capability of storing the configurations dramatically. Moreover, as will be shown in section 5.2.2 the autocorrelation time of the observables has a

β	a	$N^3 \times T$	aL [fm]
6.00	0.09314	$24^3 \times 48$	2.23536
6.10	0.07905	$28^3 \times 56$	2.21367
6.20	0.06793	$32^3 \times 64$	2.17405
6.45	0.04781	$48^3 \times 96$	2.29488

Table 5.1: Physical properties of the ensembles used for this work.

non-trivial, power-law or exponential, behavior with the lattice spacing, making the generation of the larger β ensembles even more time consuming.
The following table summarizes the final values for the parameters of the Metropolis algorithm for the different ensembles. These values have been chosen after many tests, checks of the

β	N_{conf}	N_{corr}	MC Steps	N_{hit}	$\epsilon_{SU(3)}$
6.00	1000	600	600000	30	0.25
6.10	500	600	300000	30	0.25
6.20	500	800	400000	30	0.25
6.45	250	1600	400000	30	0.25

Table 5.2: Parameters used for the generation of the ensembles on which the results of this work are based on.

autocorrelation time and mainly in an empirical way. There are some parameters that are free in principle and no real reference study on their impact on the resulting ensemble. In the next section the trial and error approach that led to this decision will be briefly discussed.
Evidently, there is less freedom on the choice of the parameters in section 4.2.5 for the gradient flow compared to section 4.1.6. The value of t_f^{MAX} is chosen in lattice units. To rescale it to physical units it must be multiplied by a^2. In the following table we report the choice of the parameters for the flow of the ensembles in section 5.1.

β	ϵ	t_f^{MAX}/a^2	$\sqrt{t_f^{MAX}}$ [fm]
6.00	0.01	10.00	0.8330
6.10	0.01	10.00	0.7070
6.20	0.01	10.00	0.6076
6.45	0.02	20.00	0.6047

Table 5.3: Parameters used for the numerical integration of the flow equations for the ensembles in section 5.1

The choice of ϵ was motivated by the work found in [35], and the same values for the combination of ϵ and t_f^{MAX}/a^2 have been chosen for all ensembles, regardless of the physical maximum smearing radius, except for the $\beta = 6.45$ case, for which the number of integration steps of the RK-MK method is kept the same, but the step size is doubled. This was needed to obtain results for large enough flow times out of the ensemble (which is by far the largest one) in reasonable computing time.

5.2 Test Runs

Running some test calculations with a completely new program is obviously necessary. First some benchmarks to check the expectation values of the observables, both on raw configurations and on flowed configurations. These benchmarks were made using 2 configurations generated with the CHROMA [36] code base from the USQCD collaboration for zero flow time observables and one configuration flowed using an extension of CHROMA called FlowOps (courtesy of T.Luu and A.Shidler ?correct?), built on QDP++ (the backbone of CHROMA), that applies the Wilson flow to configurations. Both types of tests, once all the parameters were made equal, gave results equal to machine precision with the ones generated with the new code base.
Checking the validity of expectation values of observables is a solid indication that the overall back-end of the new code-base has been implemented well, as the results are deterministic. Testing the Metropolis algorithm and assessing the quality of the generated ensembles is much harder, because it involves stochastic computations, hence no numerical check can be easily defined, one can only look at average properties of the set of configurations. Unfortunately the generation of gauge field configuration as we saw in section 4.1.6 has 3 parameters that need to be set that do affect the statistical properties of the output ensemble, mainly the autocorrelation. As it turns out however, the ϵ parameter, which controls the spread of the $SU(3)$ random elements around the identity matrix, only affects the acceptance ratio of the Metropolis test, hence the efficiency of the algorithm and not the physical properties (or at least the effects are small).
The tests were all performed on the three largest lattice spacings, as the system for the smallest one is much larger and requires a considerably longer time to compute.

5.2.1 Thermalization

When initializing the Markov Chain, to generate gauge field configurations, one has two options for the initial condition of the link variables of the lattice:

- Hot Start: all links are set to the $SU(3)$ identity element
- Cold Start: all links are set to random $SU(3)$ matrices.

It is easy to see that for the hot start the initial value for the plaquette operator would be 1, when normalized on the lattice volume. For the cold start the initial value is a random number, centered around 0. The Metropolis algorithm is supposed to drive the Markov chain towards the peak of the PDF, eq. (4.9), that is where the action has a minimum.
When computing expectation values using the Monte Carlo integration, it is important to ensure that the sampling of the observables is performed when the Metropolis algorithm reached equilibrium, when it is thermalized. In fig. 5.1 we show that only a small number of MC updates is needed to reach equilibrium (compare the thermalization time of ≈ 600 with the value of N_{corr} from section 4.1.6 and the discussion in section 5.2.2). To ensure thermalization, all results of this work are generated discarding the first 10^4 MC cycles, which is much larger than the value

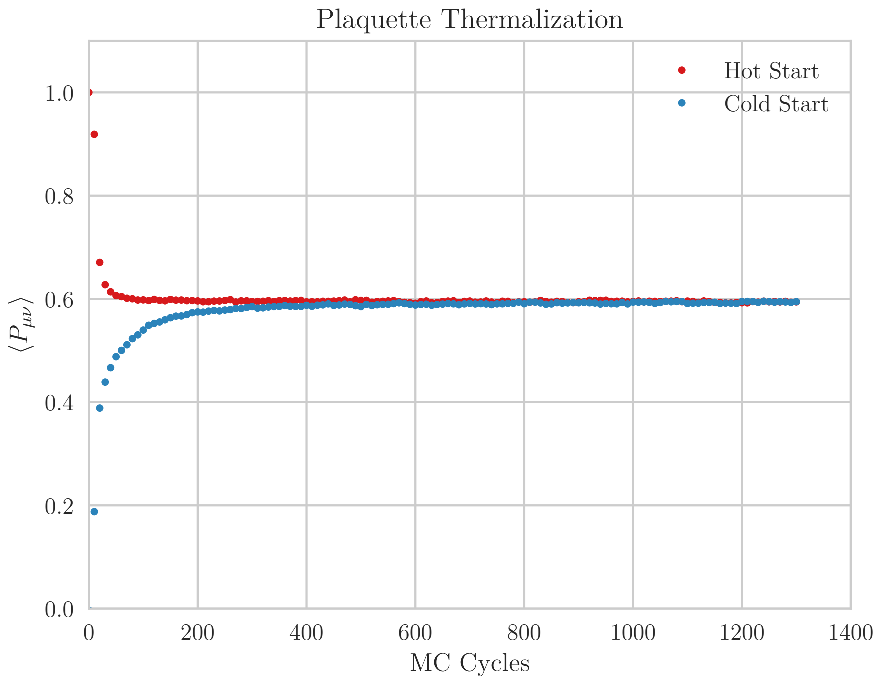

Figure 5.1: Expectation value of the Plaquette as a function of the Monte Carlo updates performed, for hot and cold starts. Equilibrium is reached in both cases after ≈ 600 updates. The data is taken from a simulation with $\beta = 6.10$.

we found, but still a small fraction, so an affordable exaggeration, of the total number of MC cycles of the Markov chain.

5.2.2 Tests for the Autocorrelation of Observables

The most important test has been the assessment of the autocorrelation time for different observables at various lattice spacings varying the parameters of the generation algorithm. As expected, the most problematic quantity is the topological charge, especially at large flow times. A good measure of how much a data series is autocorrelated is the integrated autocorrelation time τ_{int}, see section A.2, which is expected to be $1/2$ if the data is uncorrelated. In general, a larger τ_{int} implies an underestimation of uncertainties, so the variance of a quantity is corrected as $\tilde{\sigma}^2 = 2\tau_{int}\sigma^2$.
The first test, in fig. 5.2 shows the integrated autocorrelation time for the topological charge at fixed $N_{corr} = 200$ and $N_{hit} = 10$ for different lattice spacings:

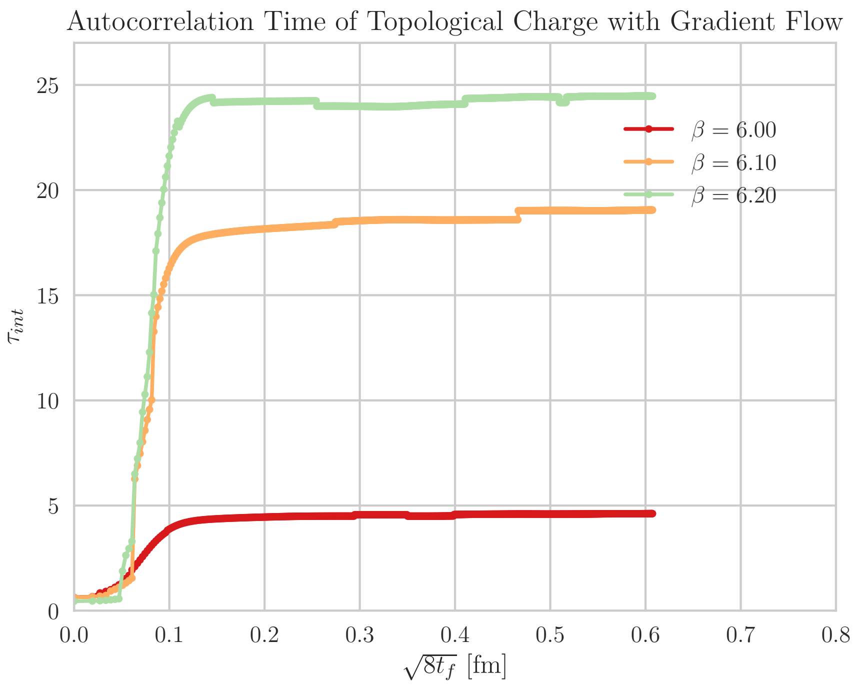

Figure 5.2: Integrated autocorrelation time for $N_{corr} = 200$ and $N_{hit} = 10$ for different inverse coupling values.

Afterwards we looked at a single lattice spacing and tried to vary the parameters N_{corr} and N_{hits} for the $\beta = 6.10$ case. From the first plot it is clear that the values that were guessed for the parameters N_{corr} and N_{hit}, which could be acceptable for the lowest beta value, are not at all fine for the other lattice spacings. On a general note we observe how the flow quickly removes the low range noise from the observable through the smearing, making it clear that the

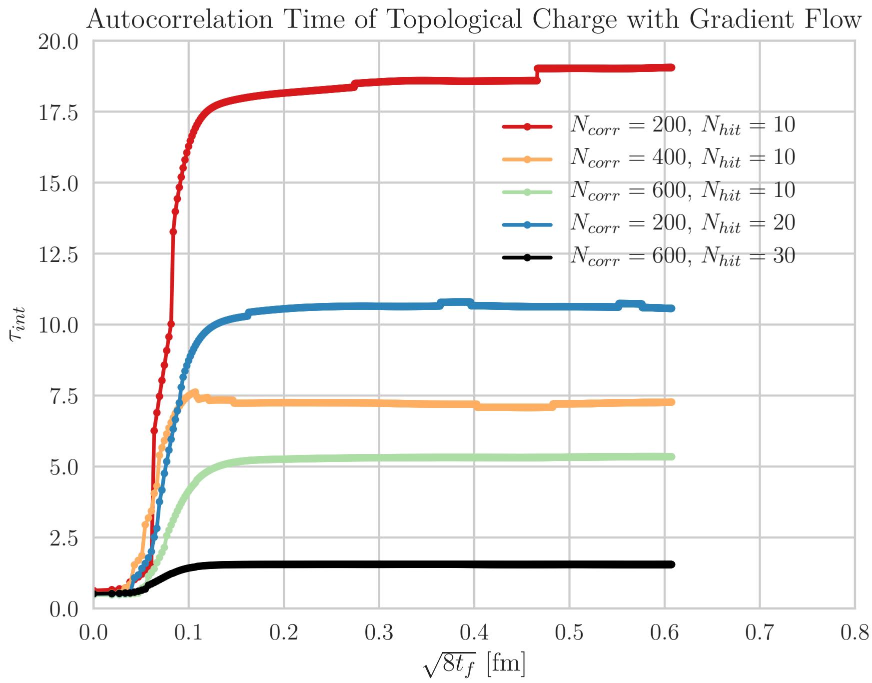

Figure 5.3: Integrated autocorrelation time for $\beta = 6.10$ as the parameters for the gauge field generation N_{corr} and N_{hit} are modified. The black data series represents the chosen set of parameters.

topological charge is highly correlated in Monte Carlo time even though it might seem uncorrelated if one only looks at $t_f = 0$.
On the other hand, fig. 5.3 suggests a possible cure for the autocorrelation issue. It is almost tautological that increasing the value of N_{corr} decreases the autocorrelation, as the parameter represents how many MC updates are performed between two measurements of the observable. The dependence of τ_{int} from N_{hits} is also clear. From the data we observed that increasing both parameters improved the autocorrelation, so the choice was to set both to a larger value from our initial guess and this proved to be the right choice. The black data series in fig. 5.3 is the data that we used for our analysis, one can notice that it is still autocorrelated, but that can be handled with a reasonable correction to the variance on the data.
It is important to stress again that the autocorrelation is a huge problem mainly for the topological charge. The energy density operator is much less affected and for all the ensembles we generated the integrated autocorrelation time is never a value much greater that 1/2 (see fig. 6.5).

5.2.3 Strong and Weak Scaling

First we can look at the scaling properties of the two sections of the code. We will distinguish the analysis in the two usual quantities used in High Performance Computing for parallel programs: strong and weak scaling.
Strong scaling is the performance of a program measured in execution time as a function of the number of processors used. One would obviously expect the relation to be ideally inverse, with execution time dropping as $1/N_{procs}$, however given the overhead caused by parallelization this is seldomly the case.
Weak scaling is the measure of the performance of a program as the size of the system increases but by keeping the total workload assigned to each processor constant. This measure is important to assess the quality of the parallelization scheme as it gives insights on how much time is spent in communication as more inter-processor messages are being sent. FIG: PLOT SCALING COMMENTI...

5.3 Production Runs and Timing

All production runs were carried out on the High Performance Computing Center at Michigan State University (MSU), with the support of the Institute for Cyber-Enabled Research (iCER). Development was performed on local machines and on the small cluster SMAUG located at the Department of Physics of the University of Oslo (UiO) and some larger benchmarks were run on the Abel Computer Cluster also at UiO.
The final ensembles were generated using the parameters in table section 5.3, shows the computing resources used for the generation of all four ensembles. I HAVE TO FIND THE DATA HERE...

β	N_{procs}	Wall Time	CPU Time
6.00	1000	600	600000
6.10	500	600	300000
6.20	500	800	400000
6.45	250	1600	400000

Table 5.4: Execution times for generating ensembles from section 5.1 with parameters found in section 5.1. All the runs were performed on the iCER cluster at MSU. N_{procs} is the number of processors used for each ensemble; the Wall Time is the "wall clock" time (the time spent in the parallel execution); CPU time is the product of Wall Time and N_{procs} and represents the actual computation time spent.

Part III

Data Analysis and Results

Chapter 6

Raw Observables

In this chapter the results for simple observables obtained from the ensembles in section 5.1 are presented. Throughout the chapter, all error estimates associated to expectation values of observables have been computed using the bootstrap method, section A.1.1, which is a popular resampling method used when the sample size of a statistical population is small, as is our case. The autocorrelation, introduced by the Markov chain, is handled using the procedure found in section A.2 as a correction to the error estimate.

6.1 Plaquette and Energy Density

The plaquette, eq. (2.18), and the energy density, eq. (2.41), are tightly related as they both are estimates of the action. We have already seen in section 5.2.1 that the plaquette can be used to check whether the metropolis algorithm has thermalized in the early stages of the chain. Another test is to check the dependence of the plaquette on the β value of the gluonic action.

Since the system is expected, after thermalization, to be at equilibrium,o the sampling of the plaquette and of the energy density should be rather constant in Monte Carlo time. Figure 6.2 shows that this is indeed the case.

When applying the gradient flow the configuration is evolved towards the minimum of the action, that implies that the values for sufficiently large flow times are both lattice spacing and flow time independent. The results do indeed suggest that this is the case:

Moving to the integrated autocorrelation time for the different ensembles, which we report only for the energy as for the plaquette is almost identical. For all ensembles the value of τ_{int} never exceeds 1, meaning that the autocorrelation of the data is not large. Nevertheless, all results of this work (including fig. 6.3 and fig. 6.4) have variances corrected by $\tilde{\sigma}^2 = 2\tau_{int}\sigma^2$.

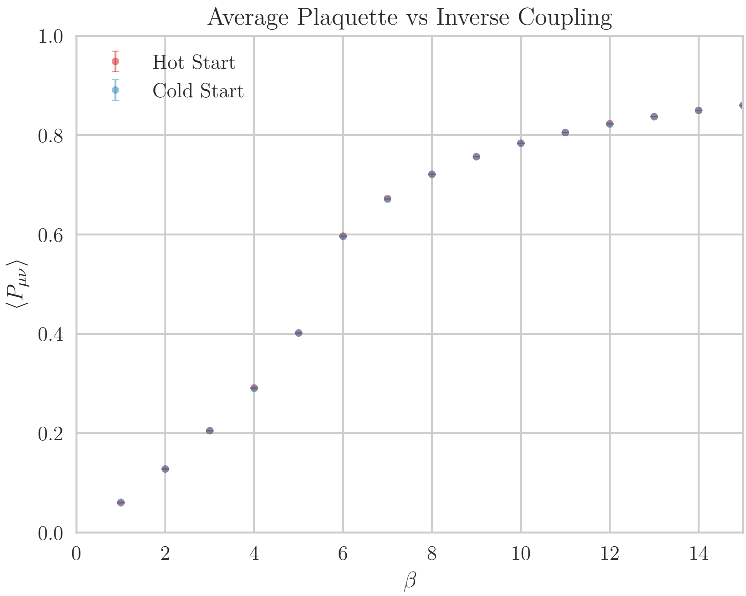

Figure 6.1: Average Plaquette value as a bunction of the inverse coupling β.

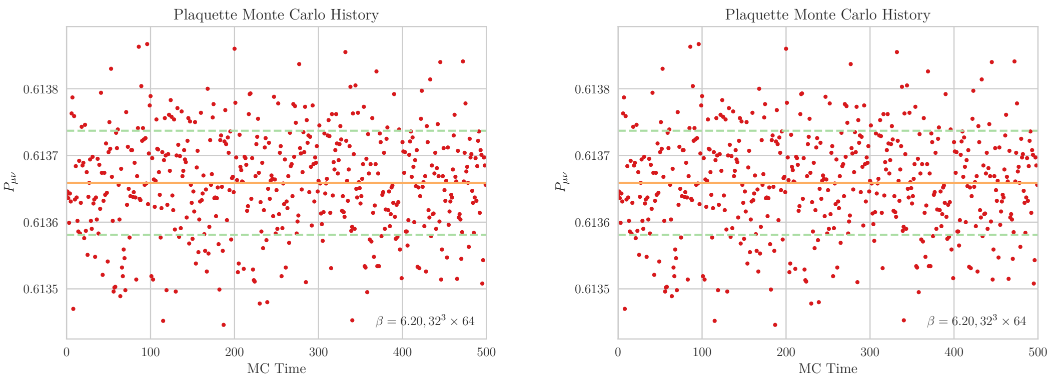

Figure 6.2: Plaquette and Energy Density as a function of Monte Carlo Time. The blue line is the average and the green dashed lines are the 1σ interval around it.

6.2 Topological Charge

A more interesting quantity to measure is the topological charge. In the continuum it is an integer, with a distribution around zero that resembles a gaussian, though there are studies that prove that indeed it is not a normal distribution [32]. The gradient flow removes the divergencies given by the discretization effect, in fig. 6.6 the flow time evolution of three of single configurations is plotted, as an example. We can notice that the value of the topological charge has a plateau at a total smearing of roughly 0.2 fm for all cases. For some configurations however, the plateau is not clear and defined. The explanation could be the too simple definition

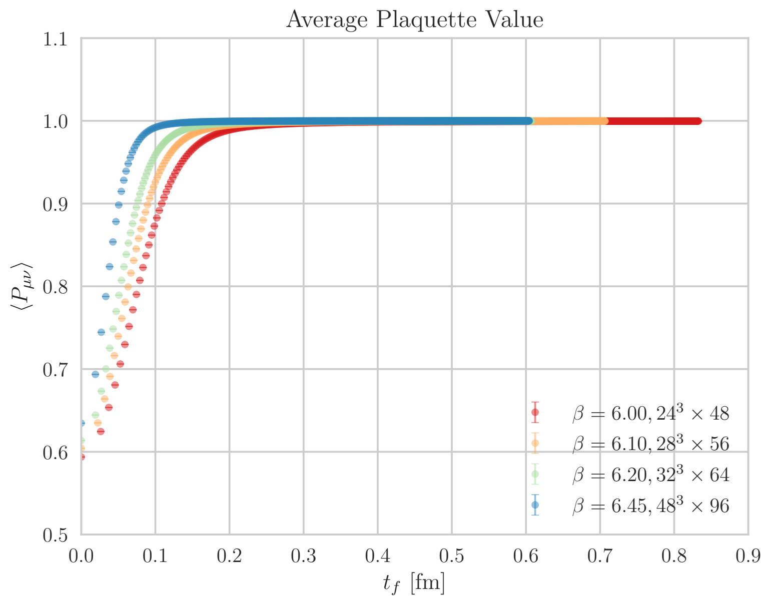

Figure 6.3: Average plaquette value as a function of flow time t_f.

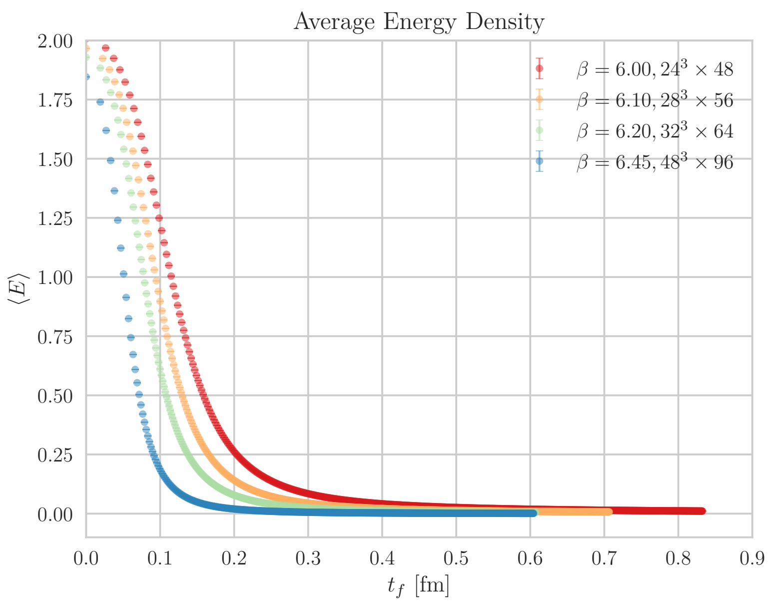

Figure 6.4: Average energy density as a function of flow time t_f.

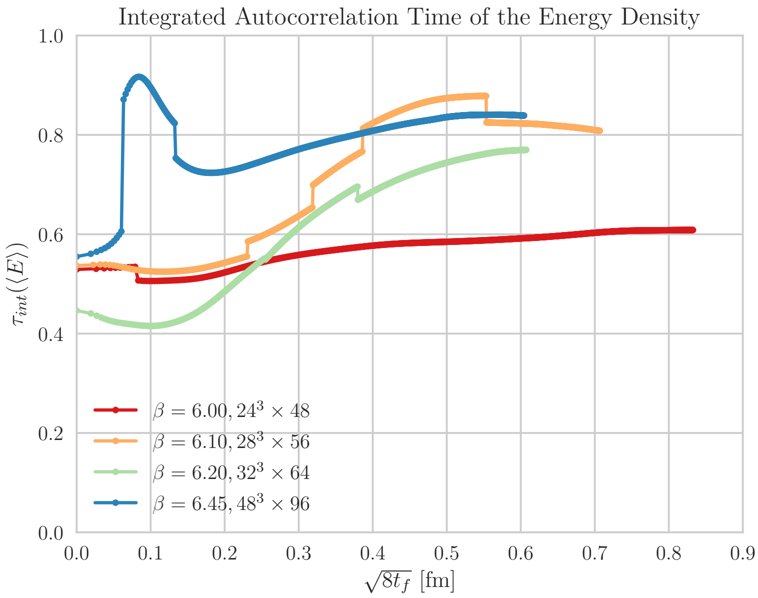

Figure 6.5: Integrated autocorrelation time of the Energy Density as a function of flow time. The discontinuity of the data is given by the approximation given by the truncation procedure described in section A.2

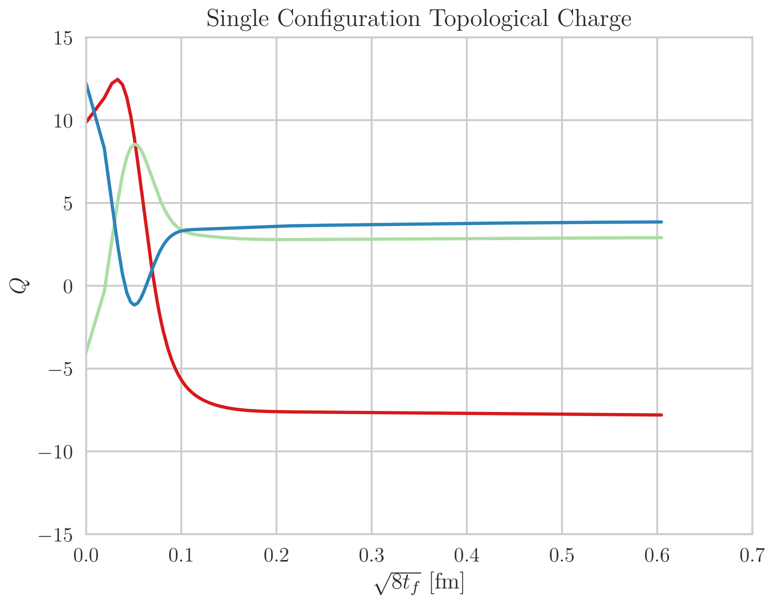

Figure 6.6: Evolution of the topological charge for three single gauge field configurations, taken at random from the $\beta = 6.10$ ensemble.

that has been used for the gauge field strength tensor. Perhaps an improved definition of the tensor, given for example with a linear combination of 1×1, 2×1, 1×2 and 2×2 (or even higher) Wilson Loops could be beneficial.

When taking the average value of the topological charge on all ensembles, we expect the average to be always zero, and from fig. 6.7 one can check that our data for the expectation value of $\mathcal{Q}$ is indeed within error-bars always compatible with zero.

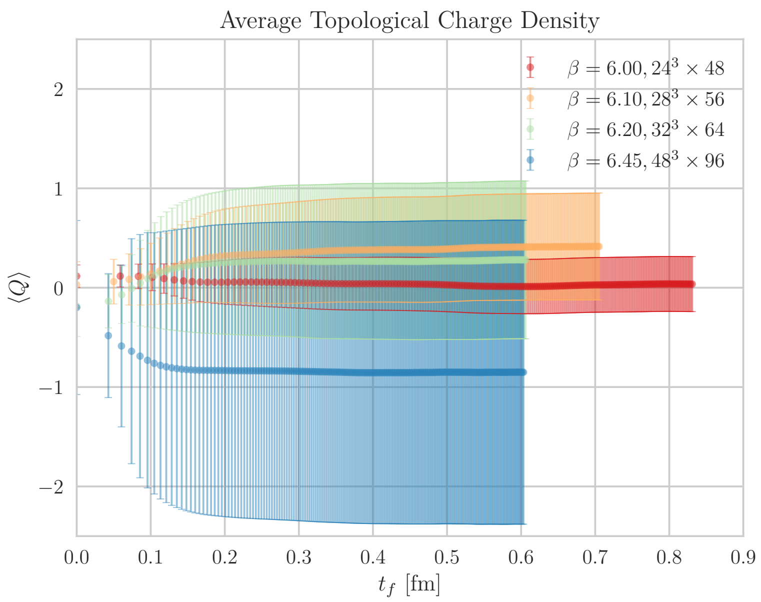

Figure 6.7: Average topological charge value as a function of flow time t_f. Errorbars are computed using bootstrap and corrected with the integrated autocorrelation time.

We should note that the increasing error-bars, for $\beta = 6.2$ and $\beta = 6.45$ in particular, are given by the decreasing ensemble size and the increasing autocorrelation time. The integrated autocorrelation time is plotted in fig. 6.8, and comparing it with the equivalent plot for the energy density (fig. 6.5) the difference is clear. The topological charge has a much larger autocorrelation time on the lattice, which grows rapidly with the inverse lattice spacing. It should be noted that the value of N_{corr} is much larger for the $\beta = 6.45$ case than all the others, but still the τ_{int} larger by far.

One last interesting consideration on the topological charge is the distribution of the large flow time value, that is the value it plateaus at. The bins are taken to be centered on integer and half-integer values in order to capture differences of the distribution of the topological charge. On the lattice it can have also not integer values, but from fig. 6.9 it is possible to see that most of the values, especially at large flow time (right histogram), are closer to the integer rather to half-integers.

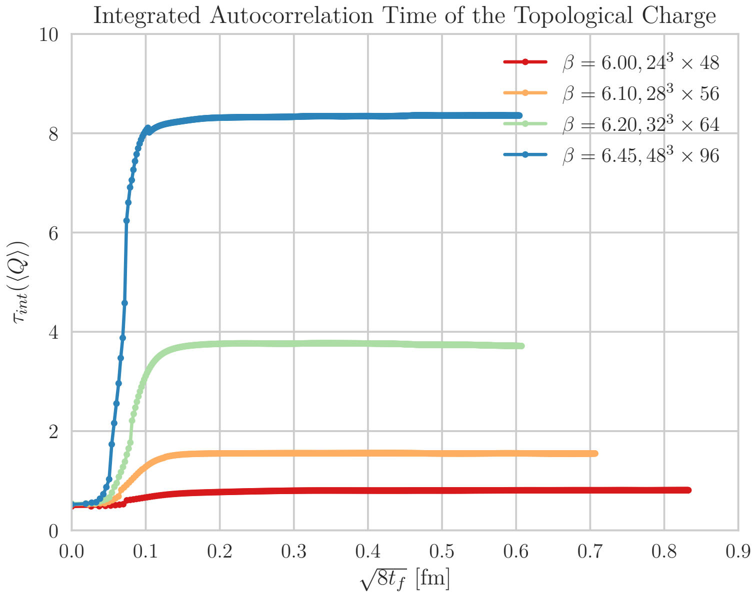

Figure 6.8: Integrated autocorrelation time of the topological charge as a function of flow time. The ensembles are the ones reported in section 4.1.6, so they have not equal number of cycles between each data point in MC time.

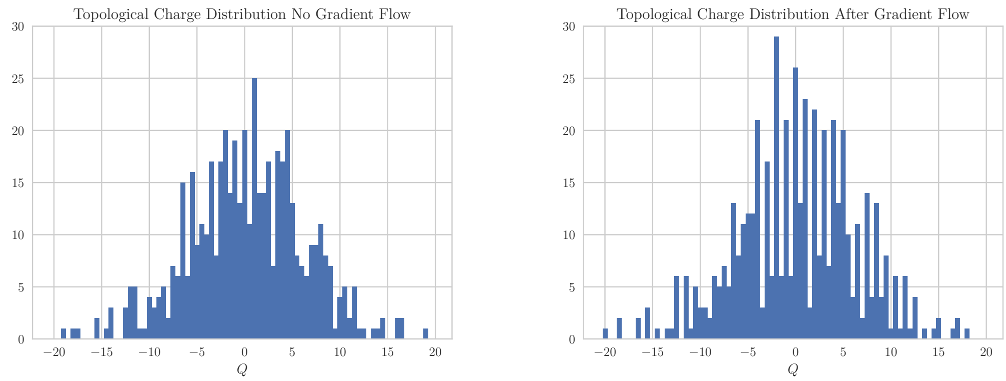

Figure 6.9: Histograms of the topological charge values at $t_f = 0$ (left) and $t_f = 0.6$ (right) for the $\beta = 6.20$ ensemble. The bins are centered on integers and half-integer values.

6.3 Topological Susceptiblity

Another quantity that is interesting to measure is the topological susceptibility. Being the average of the squared topological charge it is related to the width of the distributions in fig. 6.9. The evolution with the gradient flow of the suceptibility is not trivial. Its value at non-zero flow time does not need renormalization, as for all previously mentioned gluonic observables, but at low flow times the high-frequency fluctuations in the topological charge make it diverge.

In order to find the value that effectively reproduces the physical value in the continuum theory one must take the continuum limit.

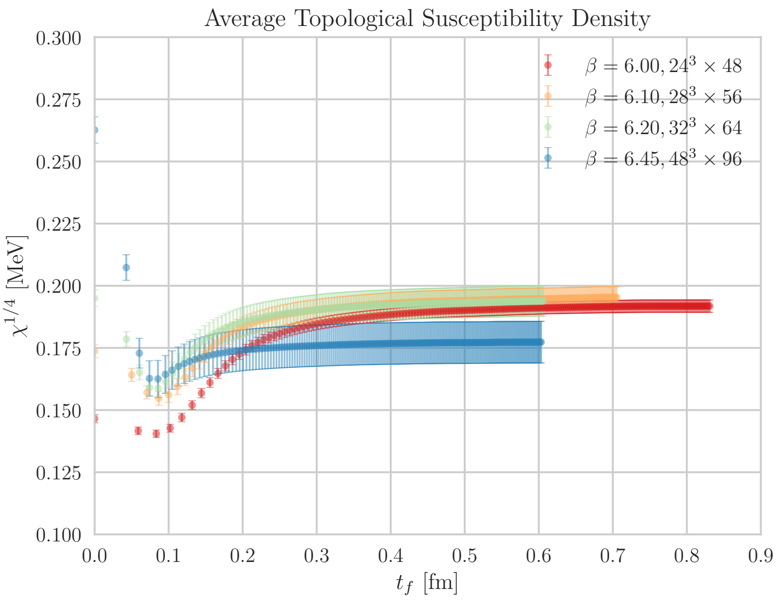

Figure 6.10: Average topological charge value as a function of flow time t_f. Errorbars are computed using bootstrap and corrected with the integrated autocorrelation time.

Here we can see the value of $\chi^{\frac{1}{4}} = \langle Q^2 \rangle^{\frac{1}{4}}$ which in physical units is an energy hence reported in MeV. We notice the fluctuations for low flow times are removed by the gradient flow. It is then possible to take the continuum limit in a region between 0.4 fm and 0.6 fm. The behavior at zero flow time is not what we were expecting, comparing for example to [37] we don't observe a clear divergency at $\sqrt{8t_f} = 0$. The behavior seems to be more more divergent (a true divergency is impossible, it is always a finite quantity on the lattice) for larger values of β. This could be due to the usage of the clover definition of the gauge field strength tensor, one of the differences between this work and the reference, that perhaps removes low distance noise from the lattice, which contributes to an oversampling of the low topological charge values. This behavior should be investigated SHOULD I REF MATHIAS'S WORK? .
When taking the continuum limit we recover the following value, taken by considering the value of the susceptibility around $\sqrt{8t_f} = 0.5$:

$$\chi^{\frac{1}{4}} = 186.9(4.9) \text{ MeV} \tag{6.1}$$

This is compatible with the value in [37] of $\chi_{ref}^{\frac{1}{4}} = 195.9(4.9)$ MeV. As an additional result we can use this extrapolation to compute the mass of the η' meson taken from the Witten-Veneziano formula:

$$\chi = \frac{F_\pi^2 m_{\eta'}^2}{2N_{flavors}} \tag{6.2}$$

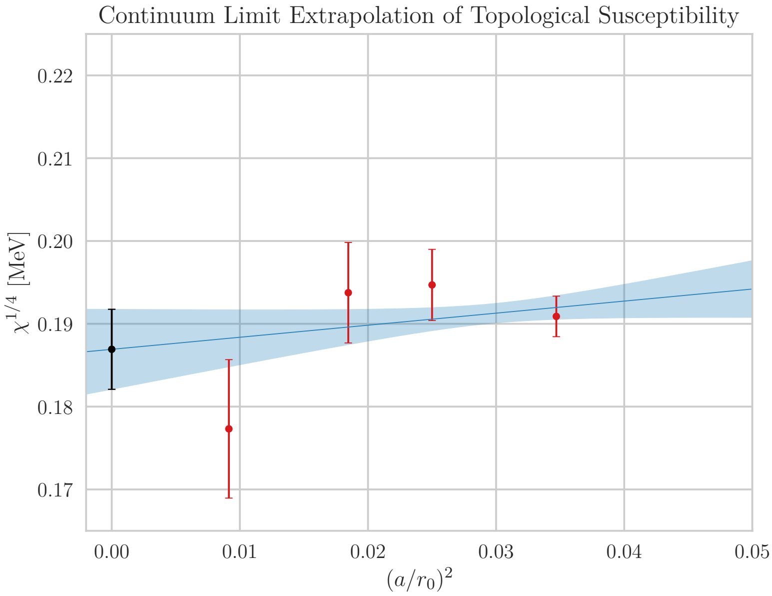

Figure 6.11: Continuum limit extrapolation of $\chi^{\frac{1}{4}}$. The black point is the extrapolated point.

Using as inputs $F_\pi = 92$ MeV, the pion decay constant, and having $N_{flavors} = 3$ naturally, the η' mass is:

$$m_{\eta'}^{(lattice)} = \sqrt{\frac{\chi^{\frac{1}{4}} 2N_{flavors}}{F_\pi^2}} = 921(16)\text{ MeV} \tag{6.3}$$

which we compare with an experimental value $m_{\eta'}^{(exp)} = 957.78(6)$ MeV, so we are off by more than 2σ, but probably the result is largely influenced by the data point obtained from $\beta = 6.45$, which has less statistics (only 250 configurations) and larger uncertainty.

Chapter 7

Running Coupling and Scale Fixing

In section 3.3 the perturbative behavior of the expectation value of $t_f^2\langle E\rangle$ was introduced. In this chapter the same quantity is studied from the data generated from our ensembles of lattice gauge field configurations, for which the code-base was developed. The matching between the perturbative and lattice results will also be discussed.

7.1 Discretization Effects on $t_f^2\langle E\rangle$

Plotting the data for the average value of the energy as a function of the dimensionless quantity t_f/r_0^2 ($r_0 = 0.5$ is the Sommer parameter, described in section 3.3.1 and has unit of length) many interesting properties can be observed. Firstly, the data suggests that for $t_f > 0.05r_0$ is lattice spacing independent, and so coupling independent since they are related. This allows, as it was suggested by [20] that this quantity can be used to set the reference scale of the lattice, similarly to r_0. By selecting a value for $t_f^2\langle E\rangle$ one can create a reference scale. It was proposed to use the value of 0.3, which from the plot we can see that is in the region of best matching between the different data series.
In an operative way one finds the value of the flow time t_0 for which:

$$t_0\langle E\rangle = 0.3 \tag{7.1}$$

This value, in this work, is found by selecting the 20 points, for each data series corresponding to a different β value, and fitting a straight line through them. By inverse regression the value of t_0 and its uncertainty are found.
We can then to check the validity of the assumptions, plot the analog of fig. 3.3 in which the ratio of $\sqrt{8t_0}/r_0$, that is the rate of the tentative scale based on the gradient flow and the Sommer parameter. If this ratio is independent from the lattice spacing then $\sqrt{8t_0}$ can be used as a reference scale r_0. With this procedure we fix a value of $\sqrt{8t_0}/r_0$ to be:

$$\sqrt{8t_0}/r_0 = 0.9499(8) \tag{7.2}$$

which is very close to the value found in [32] of $(\sqrt{8t_0}/r_0)_{ref} = 0.941(7)$.

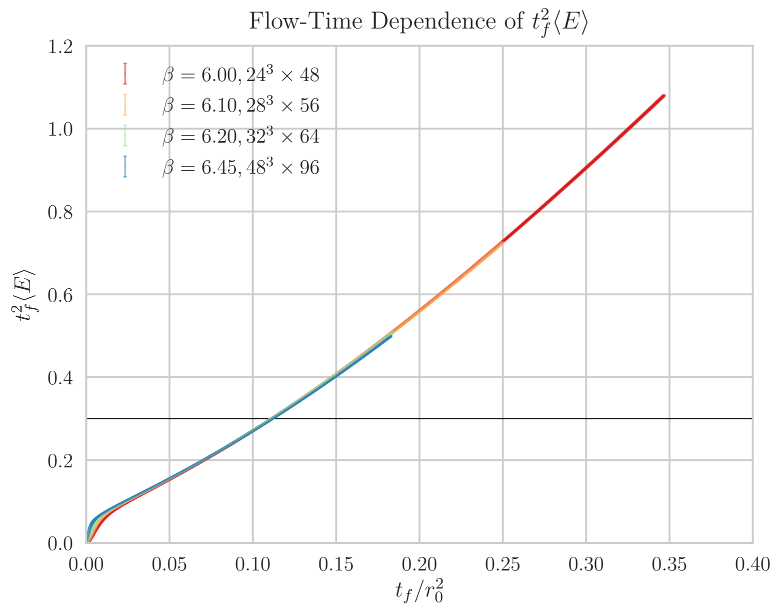

Figure 7.1: $t_f^2\langle E\rangle$ computed on the four ensembles that were generated (section 4.1.6) as a function of the flow time in units of r_0^2. The solid line is for $t_f^2\langle E\rangle = 0.3$

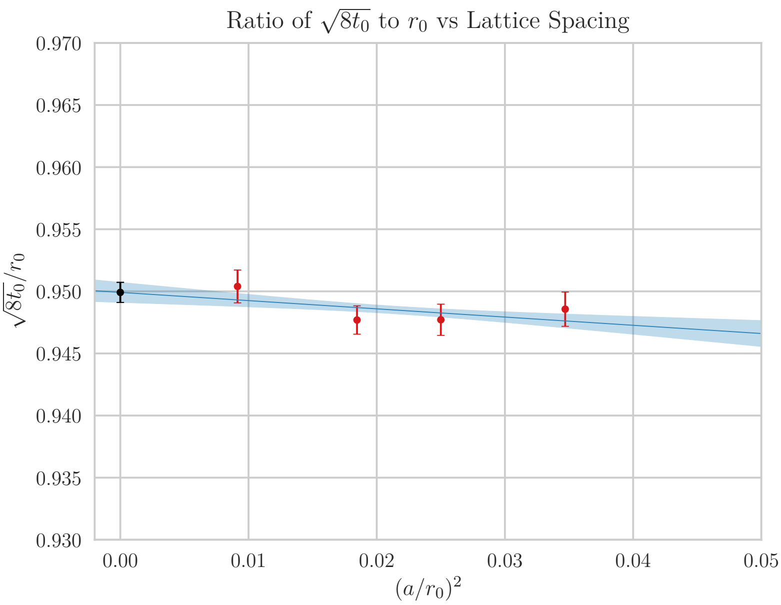

Figure 7.2: Continuum limit extrapolation of the ratio $\sqrt{8t_0}/r_0$. The solid line is the linear fit of the data points, each representing a different β value. The errorband is the 1σ confidence interval and the black point is the extrapolated continuum point.

7.2 Matching Perturbative and Lattice Results

When focusing on the low flow time section of the $t_f^2\langle E\rangle$ plot, one can study the matching between the perturbative expansion of the observable, performed in [20], and the lattice results that we generated.
The greatest challenge however is that the flow time interval in which this matching happens is unknown. Certainly for large t_f perturbation theory fails to describe the system: any perturbative expansion in $\alpha_s(q)$ becomes meaningless, as $q = 1/\sqrt{8t_f}$ becomes small the coupling grows and approaches one. For small flow times the lattice results become unreliable, in the region where the smearing radius is much smaller than the lattice spacing; this is clear by looking at a zoomed version of fig. 7.1. Both of these two bounds, no matter how intuitive they appear, are also not clearly defined and so no unique procedure can be found to constrain the matching region.

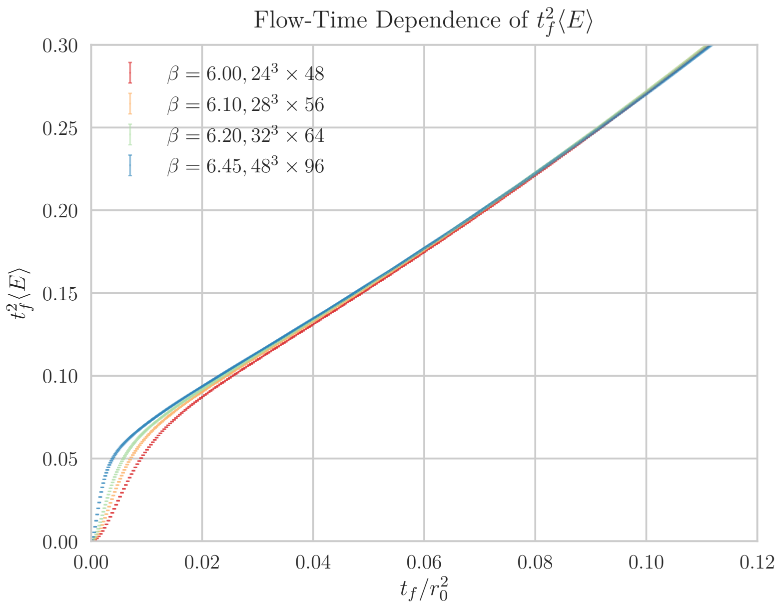

Figure 7.3: Detail of fig. 7.1 for small flow times.

7.2.1 Strategy for the Estimation of the Scale Energy Λ

The problem we are interested to solve is to extract the value of the scale energy of Yang-Mills theory from the lattice data. The only link between the two is eq. (3.19). If the equation is rewritten as:

$$t_f^2\langle E\rangle = \frac{3}{4\pi}\alpha_s(q)\left[1 + k_1\alpha_s(q) + \mathcal{O}(\alpha_s^2)\right], \qquad k_1 = 1.0978 \tag{7.3}$$

one can compute the left hand side on the lattice and fit it to the analytic expression on the right hand side from perturbation theory.

As mentioned earlier the problem is to determine matching region, which now affects the fit range. This must be done carefully in order to prevent possible biases and to assess the error on Λ properly. The first thing to do is to reconstruct the continuum limit curve for $t_f^2\langle E\rangle$. This has been done by selecting linearly spaced values of t_f/r_0^2 from 0.005 to 0.085 with spacing of $5\cdot 10^{-4}$. For each of the β values, the ten closest points around every value of the linear space were used to fit a straight line and interpolate the value of $t_f^2\langle E\rangle$ exactly on the point. An example for one of those points is shown in fig. 7.4

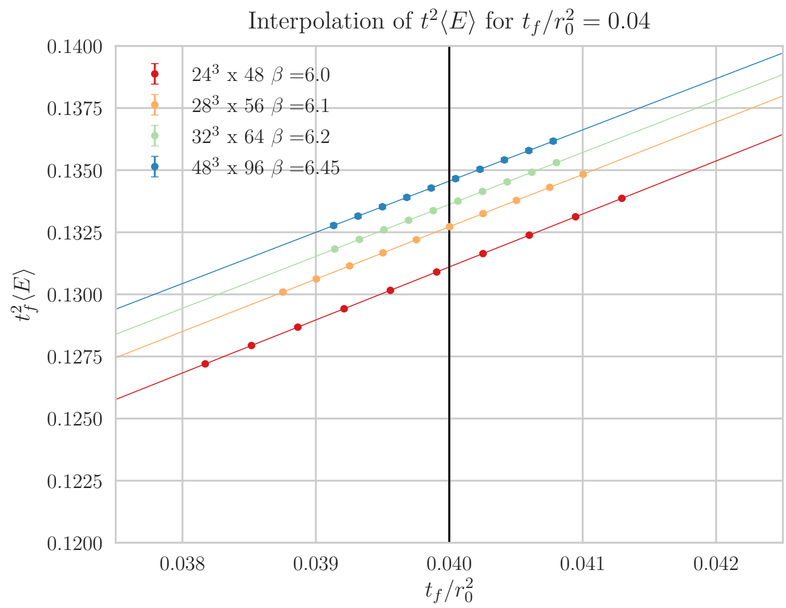

Figure 7.4: Interpolation of the lattice data for $t_f^2\langle E\rangle$ around the point $t_f/r_0^2 = 0.04$. The solid color lines represent the linear fits on the data for one β value each. The data points are the ten closest points to the desired value, represented by the black solid line.

With the interpolated data the continuum limit is taken for each value of the linear space by extrapolating the interpolated points to zero, fig. 7.5

Once this procedure is performed for all points one can plot the data series for the continuum limit. In fig. 7.6 it is plotted together with the data series from the lattice. Notice that the data is plotted against $q = \hbar c/\sqrt{8t_f}$, which is an energy. As a rough approximation, neglecting the $k_1\alpha_s^2$ term, the continuum limit plot should be proportional to the running coupling.

The estimation of the momentum scale Λ can now be performed on the continuum data. By plugging eq. (3.22), using the values of eq. (3.23) with $N_f = 0$, into eq. (7.3) one can fit the numerical data. However, the range in which to perform the fit is unknown and there is some freedom in the choice of the order of the $\alpha_s(q)$. Under such circumstances, in order to get an unbiased result for Λ a method inspired by the analysis of nucleon masses found in [38] was applied. In that paper, multiple definitions of the nucleon masses were used, but no one could be a priori be preferred over the others, and fits to multiple data with different ranges were performed; a situation somewhat resembling ours.

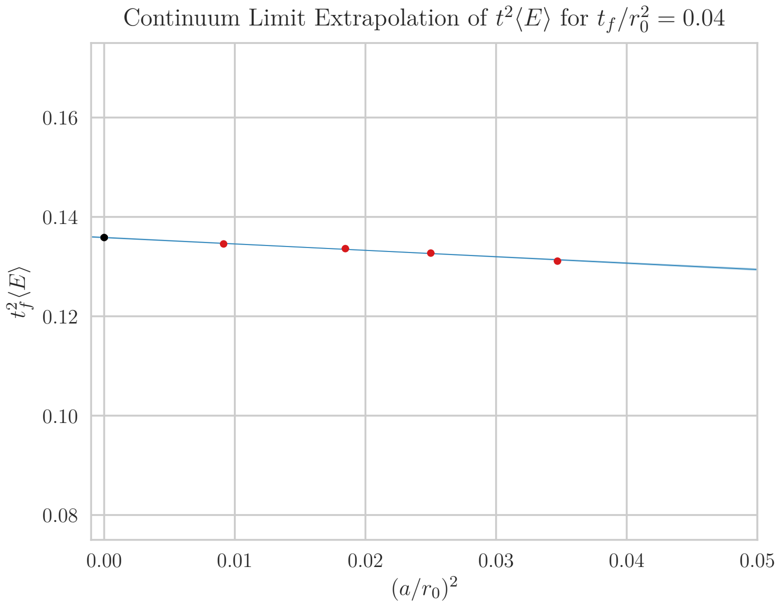

Figure 7.5: Extrapolation of the continuum limit for $t_f^2\langle E\rangle$ around the point $t_f/r_0^2 = 0.04$. The data points are the reult of the interpolation procedure in fig. 7.4.

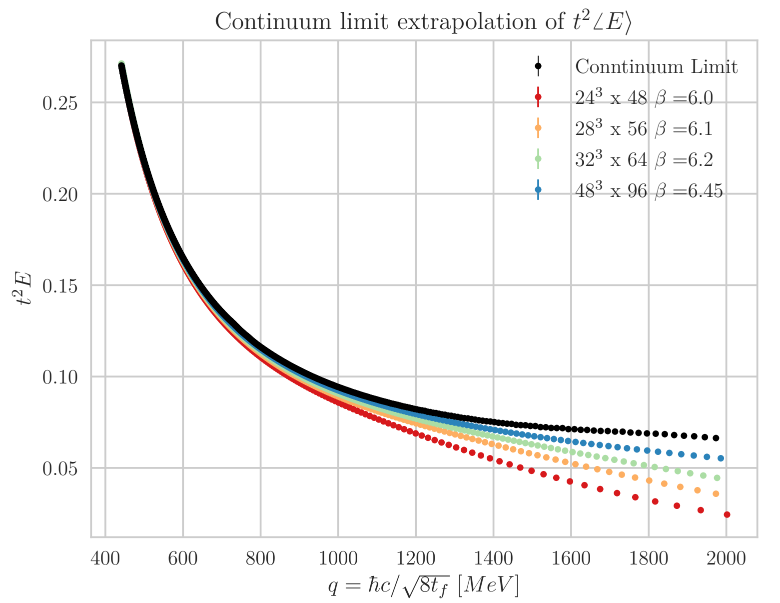

Figure 7.6: Data for $t_f^2\langle E\rangle$ from lattice observables for the ensembles in section 5.1 and the extrapolated continuum limit plotted against the energy scale $q = \hbar c/\sqrt{8t_f}$.

The key idea is to effectively perform fits between all possible fit ranges, possibly using also multiple data series if it makes sense to, and construct a histogram of the distribution of the fit parameter. The points in the distribution are then weighted with a quantity that represents the goodness of the fit and the weighted median of the points is taken as the estimator for the fit parameter.

7.3 Results for the Momentum Scale Λ

As outlined in the previous section, the aim is to estimate the momentum scale Λ by performing multiple fits of eq. (7.3). In total four different values for the momentum scale have been calculated, one for every order, from 1 to 4, of loop corrections in $\alpha_s(q)$. The difference between the various functions for the coupling are shown in fig. 7.7.

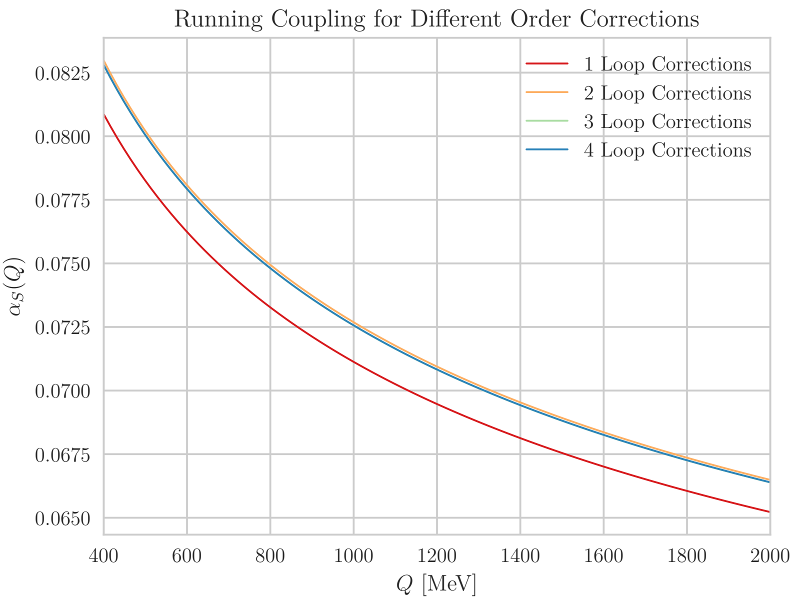

Figure 7.7: Running coupling $\alpha_s(Q)$ of pure gauge Yang-Mills theory for different loop order corrections.

The fit ranges were chosen in terms of the flow time: from $t_f/r_0^2 = 0.005$ to 0.085, of all possible lengths with minimum size 0.005. In total this gave around 3000 different fit ranges for every order of α_s.

Part IV

Conclusions

Chapter 8

Summary and Outlook

Part V

Appendices

Appendix A

Statistical Tools

The determination of the uncertainty of the results of a numerical experiment is Extremely important. In cases of small datasets, as in this work or in Lattice QCD in general, resampling methods are a popular solution for improving the estimate of the uncertainty. Another very important statistical property that is to be considered is the autocorrelation, introduced by the use of Markov chains.

A.1 Resampling: Bootstrap and Jackknife

Given a set of N measurements of an observable O, a first estimate of the expectation value and of the uncertainty are the mean and the standard deviation of the data:

$$\bar{O} = \frac{1}{N}\sum_{i=1}^{N} O_i, \qquad \sigma_O = \sqrt{\frac{1}{N}\sum_{i=1}^{N}(O_i - \bar{O})^2} \tag{A.1}$$

where O_i are the measured values of the observable. Resampling methods use the data O_i to construct multiple data series, and the average statistical properties of these series are used to estimate the properties of the original set. Both the bootstrap and the jackknife methods assume uncorrelated data. The observable O can also be a derived quantity, such as a fit on some raw data.

A.1.1 Bootstrap

The Bootstrap method consists in building N_b bootstrap samples by choosing N points at random from the the original values (repetition are allowed). The average of a bootstrap sample is then:

$$\hat{O}_b = \frac{1}{N}\sum_{i=1}^{N} O_{r(N)} \tag{A.2}$$

where $r(N)$ stands for a random number between 1 and N. One then has N_b such averages and constructs:

$$\tilde{O} = \frac{1}{N_b}\sum_{b=1}^{N_b}\hat{O}_b, \qquad \tilde{\sigma}_{\tilde{O}} = \sqrt{\frac{1}{N_b}\sum_{b=1}^{N_b}(O_b - \tilde{O})^2} \tag{A.3}$$

The expectation value of the observable is then $\langle O\rangle = \tilde{O}$ and its associated uncertainty is $\tilde{\sigma}_{\tilde{O}}$.

A.1.2 Jackknife

The Jackknife sample are not constructed at random, as is the case for bootstrap, but in a systematic manner. One creates N jackknife samples by removing for each of them the jth element of the data:

$$\hat{O}_j = \frac{1}{N-1}\sum_{i\neq j}^{N} O_i \tag{A.4}$$

One then computes:

$$\tilde{O} = \frac{1}{N}\sum_{j=1}^{N}\hat{O}_j, \qquad \tilde{\sigma}_{\tilde{O}} = \sqrt{\frac{N-1}{N}\sum_{j=1}^{N}(\hat{O}_j - \tilde{O})^2} \tag{A.5}$$

The final estimator for the expectation value is $\langle O\rangle = \tilde{O}$ and the uncertainty is $\tilde{\sigma}_{\tilde{O}}$.

Both of these resampling methods have been implemented and used; they were found to be consistent with each other. The jackknife is deterministic, the bootstrap, for sufficiently large N_b (usually $\approx$ 500 are sufficient) had error estimates compatible with jackknife and of the same order of magnitude. The error estimate when using resampling compared to the standard deviation is smaller by orders of magnitude.

A.2 Autocorrelation

The data generated via a Markov chain Monte Carlo method is always affected by autocorrelation because the data points intrinsically depend on each other. One can tune the algorithm to reduce the autocorrelation time until it becomes negligible, but this is not the case for Lattice calculations because of the computational cost involved.
We followed the procedures in [39] to get an algorithm to estimate the integrated autocorrelation time and the error correction factor due to autocorrelation.
The autocorrelation function of an ordered set variables $\{x_1, x_2, \dots x_N\}$ with expectation value $\bar{x}$ is defined as:

$$\Gamma(t) = \Gamma(-t) = \langle (x_i - \bar{x})(x_{i+t} - \bar{x})\rangle \approx \frac{1}{N-t}\sum_{i=1}^{N-t}(x_i - \bar{x})(x_{i+t} - \bar{x}) \tag{A.6}$$

where t is the "lag" between two points. The integrated autocorrelation time is given by:

$$\tau_{int} = \frac{1}{2}\sum_{t=1}^{\infty}\frac{\Gamma(t)}{\Gamma(0)} = \frac{1}{2}\sum_{t=1}^{\infty}\rho(t) \tag{A.7}$$

For sufficiently large N, the true variance of the data can be expressed as:

$$\tilde{\sigma}^2 = 2\tau_{int}\sigma^2 \tag{A.8}$$

This result is very neat, because it implies that in one can calculate the integrtated autocorrelation time correctly, the inclusion of the effects on the uncertainty estimate is trivial. In order to truncate the infinite summation in eq. (A.7) one can look at the deviation squared of $\rho(t)$, which as suggested by Sokal (CITATION NEEDED)can be written as:

$$\langle \delta\rho(t)^2 \rangle \approx \frac{1}{N}\sum_{k=1}^{\infty}[\rho(k+t)+\rho(k-t)-2\rho(k)\rho(t)]^2 \tag{A.9}$$

all these terms, for a sufficiently large value of k should all vanish, hence one can choose a cutoff Λ and truncate the sum up to $t+\Lambda$. The integrated autocorrelation time, if the deviations of $\rho(t)$ become small, plateaus, so one can truncate the sum in eq. (A.7) as well:

$$\tau_{int} = \frac{1}{2}\sum_{t=1}^{W}\rho(t) \tag{A.10}$$

where W is the first lag t for which $\rho(t) < \sqrt{(\langle \delta\rho(t)^2 \rangle}$, when the contribution to the integration of tau_{int} from that lag become smaller than the deviation of that same lag.
The integrated autocorrelation time has been computed for all quantities presented in this work and statistical uncertainties associated with results have all been corrected via eq. (A.8)

Bibliography

[1] UX: Standard model of the standard model.

[2] Schroder Peskin. *An Introduction to Quantum Field Theory*. Cambridge University Press, 1989.

[3] Shahida Dar. The neutron EDM in the SM : A review.

[4] A Chaudhuri. A short course on relativistic heavy ion collisions. 07 2012.

[5] G Dissertori. 9. QUANTUM CHROMODYNAMICS. page 50.

[6] David J. Gross and Frank Wilczek. Ultraviolet behavior of non-abelian gauge theories. *Phys. Rev. Lett.*, 30:1343–1346, Jun 1973.

[7] H. David Politzer. Reliable perturbative results for strong interactions? *Phys. Rev. Lett.*, 30:1346–1349, Jun 1973.

[8] R Machleidt and F Sammarruca. Chiral EFT based nuclear forces: achievements and challenges. 91(8):083007.

[9] S.K. Bogner, R.J. Furnstahl, and A. Schwenk. From low-momentum interactions to nuclear structure. 65(1):94–147.

[10] Kenneth G. Wilson. Confinement of quarks. 10(8):2445–2459.

[11] Christof Gattringer and Christian B. Lang. *Quantum Chromodynamics on the Lattice*, volume 788 of *Lecture Notes in Physics*. Springer Berlin Heidelberg.

[12] Rajan Gupta. Introduction to lattice QCD.

[13] E. Witten. Current algebra theorems for the u(1) goldstone boson. 156(2):269–283.

[14] Adriano Di Giacomo. Topology in lattice QCD.

[15] T. Schfer and E. V. Shuryak. Instantons in QCD. 70(2):323–425.

[16] Constantia Alexandrou, Andreas Athenodorou, Krzysztof Cichy, Arthur Dromard, Elena Garcia-Ramos, Karl Jansen, Urs Wenger, and Falk Zimmermann. Comparison of topological charge definitions in lattice QCD.

[17] David J. Gross, Robert D. Pisarski, and Laurence G. Yaffe. QCD and instantons at finite temperature. 53(1):43–80.

[18] R. Sommer. A new way to set the energy scale in lattice gauge theories and its application to the static force and α_s in SU(2) yang–mills theory. 411(2):839–854.

[19] M. Guagnelli, R. Sommer, and H. Wittig. Precision computation of a low-energy reference scale in quenched lattice QCD. 535(1):389–402.

[20] Martin Lscher. Properties and uses of the wilson flow in lattice QCD. 2010(8).

[21] Martin Lscher and Peter Weisz. Perturbative analysis of the gradient flow in non-abelian gauge theories. 2011(2).

[22] Martin Lscher. Chiral symmetry and the yang–mills gradient flow. 2013(4).

[23] Hank Childs, Eric Brugger, Brad Whitlock, Jeremy Meredith, Sean Ahern, David Pugmire, Kathleen Biagas, Mark Miller, Cyrus Harrison, Gunther H. Weber, Hari Krishnan, Thomas Fogal, Allen Sanderson, Christoph Garth, E. Wes Bethel, David Camp, Oliver Rübel, Marc Durant, Jean M. Favre, and Paul Navrátil. VisIt: An End-User Tool For Visualizing and Analyzing Very Large Data. In *High Performance Visualization–Enabling Extreme-Scale Scientific Insight*, pages 357–372. Oct 2012.

[24] Martin Lscher. Erratum: Properties and uses of the wilson flow in lattice QCD. 2014(3).

[25] G Dissertori. 9. QUANTUM CHROMODYNAMICS. page 50.

[26] T. van Ritbergen, J. A. M. Vermaseren, and S. A. Larin. The four-loop beta-function in quantum chromodynamics. 400(3):379–384.

[27] Nicholas Metropolis, Arianna W. Rosenbluth, Marshall N. Rosenbluth, Augusta H. Teller, and Edward Teller. Equation of state calculations by fast computing machines. 21(6):1087–1092.

[28] Hjorth-Jensen M. *Computational Physics, Lecture Notes*. 2015.

[29] Hans Munthe-Kaas. Runge-kutta methods on lie groups. 38(1):92–111.

[30] Hans Munthe-Kaas. Lie-butcher theory for runge-kutta methods. 35(4):572–587.

[31] Elena Celledoni, Hkon Marthinsen, and Brynjulf Owren. An introduction to lie group integrators basics, new developments and applications. 257:1040–1061.

[32] Marco C, Cristian Consonni, Georg P. Engel, and Leonardo Giusti. Non-gaussianities in the topological charge distribution of the SU(3) yang-mills theory. 92(7).

[33] Colin Morningstar and Mike Peardon. Analytic smearing of SU (3) link variables in lattice QCD. 69(5).

[34] nlohmann/json: JSON for modern c++.

[35] Marco C, Cristian Consonni, Georg P. Engel, and Leonardo Giusti. Testing the witten-veneziano mechanism with the yang-mills gradient flow on the lattice. page 353. Sissa Medialab.

[36] Robert G. Edwards and Blint Jo. The chroma software system for lattice QCD. 140:832–834.

[37] Andrea Shindler, Thomas Luu, and Jordy de Vries. The nucleon electric dipole moment with the gradient flow: the θ-term contribution. 92(9).

[38] S. Durr, Z. Fodor, J. Frison, C. Hoelbling, R. Hoffmann, S. D. Katz, S. Krieg, T. Kurth, L. Lellouch, T. Lippert, K. K. Szabo, and G. Vulvert. Ab-initio determination of light hadron masses. 322(5905):1224–1227.

[39] A. Sokal. Monte carlo methods in statistical mechanics: Foundations and new algorithms. In Cecile DeWitt-Morette, Pierre Cartier, and Antoine Folacci, editors, *Functional Integration*, volume 361, pages 131–192. Springer US.